Hydrodynamic escape of reduced proto-atmospheres on Mars and Earth

(火星・地球における還元型原始大気の流体力学的散逸)

吉田　辰哉

北海道大学大学院理学院

宇宙理学専攻

2021 年 3 月

Contents

Abstract

Mars and Earth may have obtained reduced proto-atmospheres enriched in H_2 and CH_4 during accretion. Such reduced proto-atmospheres would have been lost by hydrodynamic escape, but their fluxes and timescale for hydrogen depletion remain highly uncertain. The largest ambiguity in the previous numerical studies for hydrodynamic escape is the radiative loss of energy from the upper atmosphere where the outflow accelerates due to the solar XUV heating. The presence of infrared active species such as CH_4 would induce significant loss of thermal energy to space and thereby decrease escape flux. However, previous studies treated the degree of energy loss as a free parameter. On the other hand, chemical species in an escaping atmosphere would suffer photolysis under the intentive XUV environment. To estimate the evolution of proto-atmospheres of Mars and Earth correctly, precise modeling including exact radiative balance and chemical processes is required. Here we develop a one-dimensional hydrodynamic escape model which includes radiative processes and photochemical processes for a multi-component atmosphere and applied to reduced proto-atmospheres on Mars and Earth.

The escape rate of the reduced Martian atmosphere decreases more than one order of magnitude and the mass fractionation occurs more remarkably as the mixing ratio of CH_4 and CO increases primarily because of the radiative cooling by CH_4 and CO. The total amount of carbon species lost by hydrodynamic escape exceeds 10 bar equivalent to 20 bar of CO_2 when the proto-Mars obtained $\gtrsim 10$ bar of H_2 assuming that carbon species equivalent to 1 bar of CO_2 was left behind when most H_2 completed its hydrodynamic escape. The timescale for H_2 escape from H_2-CH_4-CO atmospheres becomes about one order of magnitude longer than that from pure hydrogen atmospheres especially when

the CH_4/CO ratio is high. If the proto-Mars obtained > 100 bar of H_2, the timescale for H_2 escape exceeds ~ 100 Myr, which implies that a reduced environment allowing the production of organic matter deposit may have been kept on early Mars traceable from geologic records. Our result also implies that atmospheres on Mars-sized proto-planets may have survived during the giant impact phase and contribute as a source of atmospheres on the larger terrestrial planets that have experienced proto-planet collisions.

In escaping outflow on Earth which has the deeper gravitational well, CH_4 is dissociated rapidly by direct photolysis and chemical reactions with ions in escaping outflow, whereas radiative cooling by photochemical products such as H_3^+, CH and CH_3 suppresses atmospheric escape significantly even though their concentrations are small: the heating efficiency decreases to ~ 0.05 at CH_4/H_2=0.007 and species heavier than H_2 cease to escape at $CH_4/H_2 \gtrsim 0.01$. The maximum timescale for H_2 escape to satisfy the constraints of the isotopic compositions and the amount of volatiles on the present Earth is more than several hundred million years. Our results suggest that a hydrogen-rich reduced environment had been kept and played an important role in producing warm climate and organic matters linked to the emergence of life organisms on early Earth.

The difference between hydrodynamic escape rates on Earth and that on Mars results mainly from the difference of the planetary mass and the gravity. The escape rate is larger for Mars even taking into account the weaker XUV flux due to the larger distance from the Sun. On Mars, the weak gravity allows relatively fast escape flow that makes adiabatic cooling effective, leading to the lower atmospheric temperature and inefficient radiative cooling. The more efficient hydrodynamic escape on Mars may have resulted in the observed paucity of volatiles on Mars compared to those on Earth.

Chapter 1

Introduction

A rocky proto-planet heavier than the Moon may have obtained a proto-atmosphere by impact degassing from planetary building blocks and gravitationally capture of the surrounding solar nebula gas (e.g. Saito and Kuramoto, 2018). The solar component of the proto-atmosphere consisted of mainly H_2 and He with elemental proportion the same as the Sun. The degassed component has often been considered to consist of primarily H_2O and CO_2 by referring to the compositions of carbonaceous meteorites thought to be the best analog of building blocks delivering volatiles and the typical composition of terrestrial volcanic gas today (e.g. Matsui and Abe, 1986). However, planetary building blocks containing metallic iron should have induced the production of reduced volatile species such as H_2 and CH_4 because metallic iron acted as a reductant for the degassed component (Kuramoto and Matsui, 1996; Zahnle et al., 2020). Even if metal-free, oxidized building blocks like carbonaceous meteorites accreted, the impact degassed component was likely enriched in reduced species because they contain abundant organic matters (Hashimoto et al., 2007). Therefore, proto-planets in the terrestrial planet region likely obtained reduced proto-atmospheres enriched in H_2 and CH_4.

The short accretion time of Mars constrained from the chronometry of Martian meteorites also supports the development of an H_2-rich proto-atmosphere on Mars. Judging from its size about half of the Earth's one, Mars may be a survivor of a proto-planet grown by oligarchic accretion in a short time-scale (Kokubo and Ida, 1998). Concordant

with this view, recent precise chronometry of Martian meteorites indicates that Mars had likely reached half of its present mass associated with the concurrent core-mantle differentiation within several Myrs from the formation of the oldest CAI (Dauphas and Pourmand 2011; Tang and Dauphas 2014). Such a short accretion time strongly implis that the growth of proto-Mars proceeded primarily within the solar nebula, which is estimated to have lasted for 2-10 Myr (e.g. Kita et al. 2005). Hence, proto-Mars likely obtained a reduced proto-atmosphere in which the degassed component and solar component were mixed (Saito and Kuramoto, 2018).

On the other hand, the isotopic similarity of Earth's mantle materials with the most reduced-type primitive meteorites supports the generation of an H_2-CH_4 rich proto-atmosphere on Earth over its entire accretional history. Earth is likely experienced giant impacts, the last of which may form the Moon (Chambers and Wetherill, 1998). Giant impacts that occurred mostly after the dissipation of solar nebula likely induced atmospheric escape from proto-planets to be merged to Earth, but a considerable part of their atmospheres likely survived against giant impacts (Genda and Abe, 2003; 2005). Recent analyses of isotopic compositions of Earth's materials and primitive meteorites indicate that most of Earth's building blocks were close to enstatite meteorites, possessing the most reduced oxidation state among primitive meteorites (Dauphas, 2017). If the similarity in the isotopic composition can be extended to that of the chemical composition, impact-generated vapor enriched in reduced species like H_2 and CH_4 (Kuramoto and Matsui, 1996; Zahnle et al. 2020) should accumulate on the proto-Earth.

Atmospheres with reduced compositions are promising sites for photochemical production of organic matters precursory of life (e.g. Schlesinger and Miller, 1983), and produce an early warm and wet climate under the faint young Sun (e.g. Sagan and Mullen, 1972; Ramirez and Craddock, 2018). However, the duration of such a reduced atmosphere has been estimated to be very short by most previous studies that modeled hydrodynamic atmospheric escape.

Hydrodynamic escape occurs when radiative heating of an atmosphere accelerates atmospheric radial outflow against the planetary gravity. Although this process does not

work on the present planets in the solar system, the X-ray and extreme ultraviolet (XUV) radiation from the young Sun may have induced hydrodynamic escape because the XUV flux of the early Sun is estimated to be as strong as $\sim$ 100 times the present mean flux from observations of stellar proxies of young Sun (Ribas et al., 2005). Hydrogen-rich atmospheres on relatively low-gravity rocky planets are susceptible to hydrodynamic escape with rates possibly very large compared to those of other atmospheric escape processes (Catling and Kasting, 2017).

Several numerical studies have been made on the hydrodynamic escape of pure hydrogen atmosphere supposing a solar nebula envelope on Earth and Mars (e.g. Sekiya et al., 1980; Erkaev et al., 2013; Lammer et al., 2014). Recent models including the estimated evolution of XUV flux indicate that the hydrogen atmospheres on Earth and Mars with the amount equivalent to that in the Earth's ocean escape totally within $\sim$ 10 Myr (Lammer et al., 2014; Erkaev et al., 2014).

Hydrodynamic escape may involve atmospheric species heavier than hydrogen (Hunten et al., 1987). Especially, they may have been easy to escape from Mars due to its lower gravity. Previous numerical studies have estimated the atmospheric escape rate of an oxidized Martian proto-atmosphere made of degassed H_2O and CO_2 assuming that those molecules were fully dissociated into atoms in the upper atmosphere by the intense solar XUV irradiation (Lammer et al., 2013; Erkaev et al., 2014). Their results suggest that the proto-atmosphere with the amount equivalent to $\sim$ 10 bar at the surface could have been lost completely in 10 Myr under the XUV flux 100 times the present. These results also indicated that proto-planets lost most of their atmospheres in 10 Myr (Odert et al., 2018).

Hydrodynamic escape of a reduced proto-atmosphere enriched in H_2 and CH_4 derived from impact degassing from planetary building blocks and gravitationally capture of the surrounding solar nebula gas remains poorly investigated. Infrared active molecules such as CH_4 may have significant effect on hydrodynamic escape by their radiative cooling. Lammer et al. (2014) and Erkaev et al. (2014) assumed that all molecules in the Martian H_2O-CO_2 atmosphere were fully dissociated into atoms in the upper atmosphere. But

part of molecules likely stays undissociated in the region where the vertical advection proceeds faster than photolysis. Moreover, photolysis products such as CH and CH_3 are also infrared active molecules. So far, however, the effects of molecular radiative cooling on hydrodynamic escape is uncertain. The same is true for photochemistry in an escaping atmosphere except for some previous studies on pure hydrogen atmospheres (e.g. Garcia, 2007). If the atmospheric escape rate decreases by radiative cooling, the duration of the reduced environment enriched in H_2 or CH_4 would become longer, which may have played an important role in producing warm and wet climate and serving organic matters on early Earth and Mars.

On the other hand, the amount of volatiles on the Martian surface is about two orders of magnitude smaller than that on Earth (e.g. Pepin, 1991). The difference of isotopic compositions of volatiles between Mars and Earth indicates that Mars have been affected by atmospheric escape more intensively. H, C, N and noble gases on Mars are enriched in heavier isotopes, which is likely due to fractionation by atmospheric escape. On the other hand, the isotopic compositions of carbon and nitrogen of the Earth's surface inventory are close to those of primitive meteorites which are likely analog of building blocks providing volatiles to Earth (Kerridge, 1985; Marty, 2012), which implies the present-day carbon and nitrogen on Earth have been little affected by hydrodynamic escape. A possible explanation of the difference in the amount of volatiles between Mars and Earth is the difference in the hydrodynamic escape rate between the proto-atmospheres on Mars and that on Earth.

Here, this study develop a one-dimensional hydrodynamic escape model which includes radiative cooling processes and photochemical processes for a multi-component atmosphere, and calculate the atmospheric escape rate of a reduced proto-atmosphere on Mars and Earth. Then, we estimate the evolution of proto-atmosphere constrained by the isotopic compositions and the amount of volatiles on present planets.

This paper is organized as follows. In chapter 2, our hydrodynamic escape model and the numerical procedure are described. Numerical results of hydrodynamic escape and estimated atmospheric evolution of Martian reduced proto-atmospheres and Earth's

reduced proto-atmospheres are described in chapters 3 and 4 respectively. The conclusion is summarized in chapter 5.

Chapter 2

Hydrodynamic Escape Model

2.1 Lower atmospheric composition

In this modeling, an atmosphere composed of H_2, CH_4, and/or CO at its low altitude is assumed. The details of assumed atmospheric compositions on Mars and Earth is described in Chapter 3 and 4 respectively.

2.2 Basic equations

We solved the equations of continuity and momentum and energy conservation for a multi-component gas assuming spherical symmetry,

$$\frac{\partial n_i}{\partial t} + \frac{1}{r^2}\frac{\partial (n_i u_i r^2)}{\partial r} = \omega_i, \tag{2.1}$$

$$\frac{\partial u_i}{\partial t} + u_i \frac{\partial u_i}{\partial r} = -\frac{1}{\rho_i}\frac{\partial p_i}{\partial r} - \frac{GM}{r^2} + \sum_j (u_j - u_i) n_j \mu_{ij} k_{ij}, \tag{2.2}$$

$$\frac{\partial}{\partial t}\left[\rho\left(\frac{1}{2}u^2 + E\right)\right] + \frac{1}{r^2}\frac{\partial}{\partial r}\left\{\left[\left(\frac{1}{2}u^2 + E + \frac{p}{\rho}\right)\rho u\right] r^2\right\} = -\frac{GM}{r^2}\rho u + q \tag{2.3}$$

where t is the time, r is the distance from the planetary center, n_i, ρ_i, u_i, p_i, and ω_i are the number density, mass density, velocity, partial pressure, and production rate of species i respectively, G is the gravitational constant, M is the mass of the planet, ρ, p, and E are

the total mass density, total pressure, and total specific internal energy, u is the mean gas velocity and μ_{ij} is the reduced molecular mass between species i and species j. k_{ij} is the momentum transfer collision frequency that follows

$$k_{ij} = \frac{k_B T}{\mu_{ij} b_{ij}}, \tag{2.4}$$

where k_B is the Boltzmann constant, T is the temperature and b_{ij} is the binary diffusion coefficient (Zahnle et al., 1990). We use

$$b_{ij} = \begin{cases} 1.96 \times 10^6 \frac{T^{1/2}}{\mu_{ij}^{1/2}} & \text{for neutral-neutral pair} \\ 4.13 \times 10^{-8} \frac{T}{\mu_{ij}^{1/2} \alpha^{1/2}} & \text{for neutral-ion pair} \\ 8.37 \times 10^{-5} \frac{T^{5/2}}{\mu_{ij}^{1/2}} & \text{for ion-ion pair} \end{cases} \tag{2.5}$$

where α is the polarizability (Banks and Kocharts, 1973; Garcia, 2007). Here, b_{ij}, T, μ_{ij} and α are expressed in $\mathrm{cm^{-1}\,s^{-1}}, \mathrm{K}, \mathrm{g}$ and $\mathrm{cm^3}$, respectively. The specific internal energy of species i follows,

$$E_i = \frac{1}{\gamma_i - 1} \frac{p_i}{\rho_i}, \tag{2.6}$$

where γ_i is the ratio of specific heats of species i. We assume that $\gamma_i = 3/2$, $7/5$, $4/3$ for monoatomic gases, diatomic gases, and multiatomic gases. The total specific internal energy is given by

$$\rho E = \sum_i \rho_i E_i = \sum_i \frac{1}{\gamma_i - 1} p_i = \frac{1}{n} \left(\sum_i \frac{n_i}{\gamma_i - 1} \right) p \equiv k_\gamma p \tag{2.7}$$

where

$$k_\gamma = \frac{1}{n} \left(\sum_i \frac{n_i}{\gamma_i - 1} \right). \tag{2.8}$$

The net heating rate is given by

$$q = q_{\mathrm{abs}} - q_{\mathrm{ch}} - q_{\mathrm{rad}} \tag{2.9}$$

where q_{abs} is the heating rate by XUV absorption, q_{ch} is the rate of net chemical expense of energy, and q_{rad} is the radiative cooling rate by infrared active molecules.

2.3 Photochemical processes

157 photochemical reactions (Table 2.1) are considered for 23 atmospheric components: H_2, CH_4, CO, H, C, O, CH, CH_2, CH_3, H^+, H_2^+, H_3^+, C^+, O^+, CO^+, CH^+, CH_2^+, CH_3^+, CH_4^+, CH_5^+, HCO^+, HOC^+, and OH^+.

The photolysis rate of molecule A can be wrriten by

$$j_{\mathrm{A}} = \int_{\lambda} \sigma_{\lambda,\mathrm{A}} N_{\lambda} d\lambda, \tag{2.10}$$

where $\sigma_{\lambda,\mathrm{A}}$ is the photodissociation/photoionization cross section at wavelength λ for species A and N_λ is the XUV photon flux at wavelength λ. We refer photodissociation cross sections and photoionization cross sections provided by "PHoto Ionization/Dissociation RATES" (`http://phidrates.space.swri.edu`). The energy consumption rate by this photolysis is given by

$$q_{\mathrm{dis,A}} = j_{\mathrm{A}} n_{\mathrm{A}} \frac{hc}{\lambda_{\mathrm{th}}}, \tag{2.11}$$

where n_{A} is the number density of species A, λ_{th} is the threshold wavelength for the photolysis, h is the Planck constant, and c is the speed of light in vacuum.

The bimolecular reaction rate can be written by

$$f_{\mathrm{R}} = k_{\mathrm{R}} n_i n_j, \tag{2.12}$$

where k_{R} is the reaction rate coefficient, and n_i, n_j are the number densities of reactants i, j respectively. We refer the photochemical reactions and these rate coefficients provided by "The UMIST Database for Astrochemistry 2012" (`http://udfa.ajmarkwick.net`). We neglect the formation of molecules which have more than one carbon. The energy consumption rate by this bimolecular reaction is given by

$$q_{\mathrm{ch,R}} = -f_{\mathrm{R}} \Delta E_{\mathrm{ch,R}}, \tag{2.13}$$

where $\Delta E_{\mathrm{ch,R}}$ is the heat of reaction, positive for endothermic reactions and negative for exothermic reactions. In the evaluation of the heats of reaction we make use of the enthalpies of formation listed in Le Teuff et al. (2000). The energy consumption rate q_{ch} is calculated by summing the consumed energy by each photochemical reaction.

Table 2.1 Photochemical reactions

No.	Reaction			Reaction rate $cm^3\,s^{-1}$
R1	$H_2 + h\nu$	$\rightarrow$	$H + H$	
R2		$\rightarrow$	$H_2^+ + e$	
R3		$\rightarrow$	$H^+ + H + e$	
R4	$CH_4 + h\nu$	$\rightarrow$	$CH_2 + H_2$	
R5		$\rightarrow$	$CH_3 + H$	
R6		$\rightarrow$	$CH_2 + H + H$	
R7		$\rightarrow$	$CH_4^+ + e$	
R8		$\rightarrow$	$CH_3^+ + H + e$	
R9		$\rightarrow$	$CH_2^+ + H_2 + e$	
R10		$\rightarrow$	$CH^+ + H_2 + H + e$	
R11		$\rightarrow$	$H^+ + CH_3 + e$	
R12		$\rightarrow$	$CH + H_2 + H$	
R13	$CO + h\nu$	$\rightarrow$	$CO^+ + e$	
R14		$\rightarrow$	$C^+ + O + e$	
R15		$\rightarrow$	$C + O^+ + e$	
R16		$\rightarrow$	$C + O$	
R17	$H + h\nu$	$\rightarrow$	$H^+ + e$	
R18	$C + h\nu$	$\rightarrow$	$C^+ + e$	
R19	$O + h\nu$	$\rightarrow$	$O^+ + e$	
R20	$CH + h\nu$	$\rightarrow$	$CH^+ + e$	
R21	$CH + h\nu$	$\rightarrow$	$C + H$	
R22	$CH_3 + h\nu$	$\rightarrow$	$CH_3^+ + e$	
R23	$CH_3 + h\nu$	$\rightarrow$	$CH + H_2$	
R24	$CH_3 + h\nu$	$\rightarrow$	$CH_2 + H$	
R25	$H_2 + CH$	$\rightarrow$	$C + H_2 + H$	$6.00 \times 10^{-9}\exp(-40200/T)$
				Ref. McElroy et al. (2013)

Table 2.1 Photochemical reactions

No.	Reaction			Reaction rate $cm^3\,s^{-1}$
R26	$H_2 + CH$	$\rightarrow$	$CH_2 + H$	$5.46 \times 10^{-10}\exp(-1943/T)$
R27	$H_2 + H_2$	$\rightarrow$	$H_2 + H + H$	$1.00 \times 10^{-8}\exp(-84100/T)$
R28	$H + H_2$	$\rightarrow$	$H + H + H$	$4.67 \times 10^{-7}(T/300)^{-1.00}\exp(-55000/T)$
R29	$H_2^+ + H_2$	$\rightarrow$	$H_3^+ + H$	2.08×10^{-9}
R30	$H_2 + C^+$	$\rightarrow$	$CH^+ + H$	$1.00 \times 10^{-10}\exp(-4640/T)$
R31	$H_2 + C^+$	$\rightarrow$	$CH_2^+ + PHOTON$	$2.00 \times 10^{-16}(T/300)^{-1.30}\exp(-23.00/T)$
R32	$H_2 + CH^+$	$\rightarrow$	$CH_2^+ + H$	1.20×10^{-9}
R33	$H_2 + CH_2^+$	$\rightarrow$	$CH_3^+ + H$	1.60×10^{-9}
R34	$H_2 + CH_4^+$	$\rightarrow$	$CH_5^+ + H$	$4.89 \times 10^{-11}(T/300)^{-0.14}\exp(36.10/T)$
R35	$H_2 + C$	$\rightarrow$	$CH + H$	$6.64 \times 10^{-10}\exp(-11700/T)$
R36	$H_2 + C$	$\rightarrow$	$CH_2 + PHOTON$	1.00×10^{-17}
R37	$H_2 + CH_2$	$\rightarrow$	$CH_3 + H$	$5.18 \times 10^{-11}(T/300)^{0.17}\exp(-6400/T)$
R38	$H_2 + CH_3$	$\rightarrow$	$CH_4 + H$	$6.86 \times 10^{-14}(T/300)^{2.74}\exp(-4740/T)$
R39	$H_2 + CH_3^+$	$\rightarrow$	$CH_5^+ + PHOTON$	$3.92 \times 10^{-16}(T/300)^{-2.29}\exp(-21.30/T)$
R40	$H_2 + CH$	$\rightarrow$	$CH_3 + PHOTON$	$5.09 \times 10^{-18}(T/300)^{-0.71}\exp(-11.60/T)$
R41	$H_2 + CO^+$	$\rightarrow$	$HCO^+ + H$	7.50×10^{-10}
R42	$H_2 + CO^+$	$\rightarrow$	$HOC^+ + H$	7.50×10^{-10}
R43	$H_2 + O^+$	$\rightarrow$	$OH^+ + H$	1.70×10^{-9}
R44	$H_2 + HOC^+$	$\rightarrow$	$HCO^+ + H_2$	3.80×10^{-10}
R45	$H^+ + CH_4$	$\rightarrow$	$CH_4^+ + H$	1.50×10^{-9}
R46	$H^+ + CH_4$	$\rightarrow$	$CH_3^+ + H_2$	2.30×10^{-9}
R47	$H_2^+ + CH_4$	$\rightarrow$	$CH_4^+ + H_2$	1.40×10^{-9}
R48	$H_2^+ + CH_4$	$\rightarrow$	$CH_3^+ + H_2 + H$	2.30×10^{-9}
R49	$H_2^+ + CH_4$	$\rightarrow$	$CH_5^+ + H$	1.14×10^{-10}
R50	$H_3^+ + CH_4$	$\rightarrow$	$CH_5^+ + H_2$	2.40×10^{-9}

Ref. McElroy et al. (2013)

Table 2.1 Photochemical reactions

No.	Reaction			Reaction rate $cm^3\,s^{-1}$
R51	$CH_4^+ + CH_4$	$\rightarrow$	$CH_5^+ + CH_3$	1.50×10^{-9}
R52	$CH_2 + CH_4$	$\rightarrow$	$CH_3 + CH_3$	$7.13 \times 10^{-12}\exp(-5050/T)$
R53	$CO^+ + CH_4$	$\rightarrow$	$CO + CH_4^+$	7.93×10^{-10}
R54	$O^+ + CH_4$	$\rightarrow$	$CH_4^+ + O$	8.90×10^{-10}
R55	$CO^+ + CH_4$	$\rightarrow$	$HCO^+ + CH_3$	4.55×10^{-10}
R56	$OH^+ + CH_4$	$\rightarrow$	$CH_5^+ + O$	1.95×10^{-10}
R57	$H + CH_4$	$\rightarrow$	$CH_3 + H_2$	$5.94 \times 10^{-13}(T/300)^{3.0}\exp(-4045/T)$
R58	$H_2^+ + CO$	$\rightarrow$	$CO^+ + H_2$	6.44×10^{-10}
R59	$O^+ + CO$	$\rightarrow$	$CO^+ + O$	$4.90 \times 10^{-12}(T/300)^{0.5}\exp(-4580/T)$
R60	$CH_4^+ + CO$	$\rightarrow$	$HCO^+ + CH_3$	1.40×10^{-9}
R61	$CH_5^+ + CO$	$\rightarrow$	$HCO^+ + CH_4$	1.00×10^{-9}
R62	$H_2^+ + CO$	$\rightarrow$	$HCO^+ + H$	2.16×10^{-9}
R63	$H_3^+ + CO$	$\rightarrow$	$HCO^+ + H_2$	1.70×10^{-9}
R64	$H_3^+ + CO$	$\rightarrow$	$HOC^+ + H_2$	2.70×10^{-11}
R65	$OH^+ + CO$	$\rightarrow$	$HCO^+ + O$	1.05×10^{-9}
R66	$H + CH$	$\rightarrow$	$C + H + H$	$6.00 \times 10^{-9}\exp(-40200/T)$
R67	$H + H_2^+$	$\rightarrow$	$H_2 + H^+$	6.40×10^{-10}
R68	$H + CH^+$	$\rightarrow$	$C^+ + H_2$	$9.06 \times 10^{-10}(T/300)^{-0.37}\exp(-29.10/T)$
R69	$H + CH_2^+$	$\rightarrow$	$CH^+ + H_2$	$1.00 \times 10^{-9}\exp(-7080/T)$
R70	$H + CH_3^+$	$\rightarrow$	$CH_2^+ + H_2$	$7.00 \times 10^{-10}\exp(-10560/T)$
R71	$H + CH_4^+$	$\rightarrow$	$CH_3^+ + H_2$	1.00×10^{-11}
R72	$H + CH_5^+$	$\rightarrow$	$CH_4^+ + H_2$	1.50×10^{-10}
R73	$H + CH_2$	$\rightarrow$	$CH + H_2$	2.20×10^{-10}
R74	$H + CH_3$	$\rightarrow$	$CH_2 + H_2$	$1.00 \times 10^{-10}\exp(-7600/T)$
R75	$H + CH_4$	$\rightarrow$	$CH_2 + H_2$	$5.94 \times 10^{-13}(T/300)^{3.00}\exp(-4045/T)$
				Ref. McElroy et al. (2013)

Table 2.1 Photochemical reactions

No.	Reaction			Reaction rate $cm^3\,s^{-1}$
R76	$H + CH$	$\rightarrow$	$C + H_2$	$1.31 \times 10^{-10} \exp(-80.00/T)$
R77	$H^+ + H$	$\rightarrow$	$H_2^+ + PHOTON$	$1.15 \times 10^{-18} (T/300)^{1.49} \exp(-228.0/T)$
R78	$H + C^+$	$\rightarrow$	$CH^+ + PHOTON$	1.70×10^{-17}
R79	$H + C$	$\rightarrow$	$CH + PHOTON$	1.00×10^{-17}
R80	$H + O^+$	$\rightarrow$	$O + H^+$	$5.66 \times 10^{-10} (T/300)^{0.36} \exp(8.60/T)$
R81	$H + CO^+$	$\rightarrow$	$CO + H^+$	7.50×10^{-10}
R82	$C + CH_5^+$	$\rightarrow$	$CH_4 + CH^+$	1.20×10^{-9}
R83	$C + H_2^+$	$\rightarrow$	$CH^+ + H$	2.40×10^{-9}
R84	$C + H_3^+$	$\rightarrow$	$CH^+ + H_2$	2.00×10^{-9}
R85	$C + H_3^+$	$\rightarrow$	$CH^+ + H_2$	2.00×10^{-9}
R86	$C + CO^+$	$\rightarrow$	$CO + C^+$	1.10×10^{-10}
R87	$C + HCO^+$	$\rightarrow$	$CO + CH^+$	1.10×10^{-9}
R88	$C + OH^+$	$\rightarrow$	$O + CH^+$	1.20×10^{-9}
R89	$C + O^+$	$\rightarrow$	$CO^+ + PHOTON$	$5.00 \times 10^{-10} (T/300)^{-3.70} \exp(-800/T)$
R90	$C + O$	$\rightarrow$	$CO + PHOTON$	$4.69 \times 10^{-19} (T/300)^{1.52} \exp(50.50/T)$
R91	$C + CH_2$	$\rightarrow$	$CH + CH$	$2.69 \times 10^{-12} \exp(-23550/T)$
R92	$CH + O$	$\rightarrow$	$HCO^+ + e$	$1.09 \times 10^{-11} (T/300)^{-2.19} \exp(-165.1/T)$
R93	$H^+ + O$	$\rightarrow$	$O^+ + H$	$6.86 \times 10^{-10} (T/300)^{0.26} \exp(-224.3/T)$
R94	$CO^+ + O$	$\rightarrow$	$CO + O^+$	1.40×10^{-10}
R95	$CH^+ + O$	$\rightarrow$	$CO^+ + H$	3.50×10^{-10}
R96	$CH_2^+ + O$	$\rightarrow$	$HCO^+ + H$	7.50×10^{-10}
R97	$CH_3^+ + O$	$\rightarrow$	$HCO^+ + H_2$	4.00×10^{-10}
R98	$H_2^+ + O$	$\rightarrow$	$OH^+ + H$	1.50×10^{-9}
R99	$H_3^+ + O$	$\rightarrow$	$OH^+ + H_2$	8.40×10^{-10}
R100	$CH_4^+ + O$	$\rightarrow$	$OH + CH_3^+$	1.00×10^{-9}

Ref. McElroy et al. (2013)

Table 2.1 Photochemical reactions

No.	Reaction			Reaction rate $cm^3\,s^{-1}$
R101	$CH_2 + O$	$\rightarrow$	$CO + H_2$	8.00×10^{-11}
R102	$CH_2 + O$	$\rightarrow$	$CO + H + H$	1.33×10^{-10}
R103	$CH_3 + O$	$\rightarrow$	$CO + H_2 + H$	$3.60 \times 10^{-11}\exp(-202/T)$
R104	$CH + O$	$\rightarrow$	$CO + H$	$6.02 \times 10^{-11}(T/300)^{0.10}\exp(4.5/T)$
R105	$C^+ + O$	$\rightarrow$	$CO^+ + PHOTON$	$3.14 \times 10^{-18}(T/300)^{-0.15}\exp(-68/T)$
R106	$C^+ + CH$	$\rightarrow$	$CH^+ + C$	$3.80 \times 10^{-10}(T/300)^{-0.5}$
R107	$H^+ + CH$	$\rightarrow$	$CH^+ + H$	$1.90 \times 10^{-9}(T/300)^{-0.5}$
R108	$H_2^+ + CH$	$\rightarrow$	$CH^+ + H_2$	$7.10 \times 10^{-10}(T/300)^{-0.5}$
R109	$H_2^+ + CH$	$\rightarrow$	$CH_2^+ + H$	$7.10 \times 10^{-10}(T/300)^{-0.5}$
R110	$CH_5^+ + CH$	$\rightarrow$	$CH_2^+ + CH_4$	$6.90 \times 10^{-10}(T/300)^{-0.5}$
R111	$H_3^+ + CH$	$\rightarrow$	$CH_2^+ + H_2$	$1.20 \times 10^{-9}(T/300)^{-0.5}$
R112	$CO^+ + CH$	$\rightarrow$	$CO + CH^+$	$3.20 \times 10^{-10}(T/300)^{-0.5}$
R113	$O^+ + CH$	$\rightarrow$	$O + CH^+$	$3.50 \times 10^{-10}(T/300)^{-0.5}$
R114	$CO^+ + CH$	$\rightarrow$	$HCO^+ + C$	$3.20 \times 10^{-10}(T/300)^{-0.5}$
R115	$HCO^+ + CH$	$\rightarrow$	$CH_2^+ + CO$	$6.30 \times 10^{-10}(T/300)^{-0.5}$
R116	$O^+ + CH$	$\rightarrow$	$CO^+ + H$	$3.50 \times 10^{-10}(T/300)^{-0.5}$
R117	$OH^+ + CH$	$\rightarrow$	$CH_2^+ + O$	$3.50 \times 10^{-10}(T/300)^{-0.5}$
R118	$C^+ + CH_2$	$\rightarrow$	$CH_2^+ + C$	5.20×10^{-10}
R119	$H^+ + CH_2$	$\rightarrow$	$CH_2^+ + H$	1.40×10^{-9}
R120	$H^+ + CH_2$	$\rightarrow$	$CH^+ + H_2$	1.40×10^{-9}
R121	$H_2^+ + CH_2$	$\rightarrow$	$CH_2^+ + H_2$	1.00×10^{-9}
R122	$H_2^+ + CH_2$	$\rightarrow$	$CH_3^+ + H$	1.00×10^{-9}
R123	$H_3^+ + CH_2$	$\rightarrow$	$CH_3^+ + H_2$	1.70×10^{-9}
R124	$CH_5^+ + CH_2$	$\rightarrow$	$CH_4 + CH_3^+$	9.60×10^{-10}
R125	$CH_2 + CH_2$	$\rightarrow$	$CH_3 + CH$	$4.00 \times 10^{-10}\exp(-5000/T)$

Ref. McElroy et al. (2013)

Table 2.1 Photochemical reactions

No.	Reaction			Reaction rate $\mathrm{cm^3\,s^{-1}}$
R126	$CH_2 + O^+$	$\rightarrow$	$O + CH_2^+$	9.70×10^{-10}
R127	$CH_2 + CO^+$	$\rightarrow$	$CO + CH_2^+$	4.30×10^{-10}
R128	$CH_2 + CO^+$	$\rightarrow$	$HCO^+ + CH$	4.30×10^{-10}
R129	$CH_2 + HCO^+$	$\rightarrow$	$CO + CH_3^+$	8.60×10^{-10}
R130	$CH_2 + OH^+$	$\rightarrow$	$O + CH_3^+$	4.80×10^{-10}
R131	$H^+ + CH_3$	$\rightarrow$	$CH_3^+ + H$	3.40×10^{-9}
R132	$H_3^+ + CH_3$	$\rightarrow$	$CH_4^+ + H_2$	2.10×10^{-9}
R133	$CH_3 + CH_3$	$\rightarrow$	$CH_4 + CH_2$	$7.13 \times 10^{-12}\exp(-5052/T)$
R134	$H^+ + e$	$\rightarrow$	$H + PHOTON$	$3.50 \times 10^{-12}(T/300)^{-0.75}$
R135	$H_2^+ + e$	$\rightarrow$	$H + H$	$1.60 \times 10^{-8}(T/300)^{-0.43}$
R136	$H_3^+ + e$	$\rightarrow$	$H_2 + H$	$2.34 \times 10^{-8}(T/300)^{-0.52}$
R137	$H_3^+ + e$	$\rightarrow$	$H + H + H$	$4.36 \times 10^{-8}(T/300)^{-0.52}$
R138	$C^+ + e$	$\rightarrow$	$C + PHOTON$	$2.36 \times 10^{-12}(T/300)^{-0.29}\exp(17.60/T)$
R139	$O^+ + e$	$\rightarrow$	$O + PHOTON$	$3.24 \times 10^{-12}(T/300)^{-0.66}$
R140	$CH^+ + e$	$\rightarrow$	$C + H$	$1.50 \times 10^{-7}(T/300)^{-0.42}$
R141	$CH_2^+ + e$	$\rightarrow$	$C + H_2$	$7.68 \times 10^{-8}(T/300)^{-0.60}$
R142	$CH_2^+ + e$	$\rightarrow$	$C + H + H$	$4.03 \times 10^{-7}(T/300)^{-0.60}$
R143	$CH_2^+ + e$	$\rightarrow$	$CH + H$	$1.60 \times 10^{-7}(T/300)^{-0.60}$
R144	$CH_3^+ + e$	$\rightarrow$	$CH_2 + H$	$7.75 \times 10^{-8}(T/300)^{-0.50}$
R145	$CH_3^+ + e$	$\rightarrow$	$CH + H_2$	$1.95 \times 10^{-7}(T/300)^{-0.50}$
R146	$CH_3^+ + e$	$\rightarrow$	$CH + H + H$	$2.00 \times 10^{-7}(T/300)^{-0.40}$
R147	$CH_4^+ + e$	$\rightarrow$	$CH_2 + H + H$	$1.75 \times 10^{-7}(T/300)^{-0.50}$
R148	$CH_4^+ + e$	$\rightarrow$	$CH_3 + H$	$1.75 \times 10^{-7}(T/300)^{-0.50}$
R149	$CH_5^+ + e$	$\rightarrow$	$CH_2 + H_2 + H$	$4.76 \times 10^{-8}(T/300)^{-0.52}$
R150	$CH_5^+ + e$	$\rightarrow$	$CH_3 + H_2$	$1.40 \times 10^{-8}(T/300)^{-0.52}$

Ref. McElroy et al. (2013)

Table 2.1 Photochemical reactions

No.	Reaction			Reaction rate $\mathrm{cm^3\,s^{-1}}$
R151	$CH_5^+ + e$	$\rightarrow$	$CH_3 + H + H$	$1.96 \times 10^{-7}(T/300)^{-0.52}$
R152	$CH_5^+ + e$	$\rightarrow$	$CH_4 + H$	$1.40 \times 10^{-8}(T/300)^{-0.52}$
R153	$CH_5^+ + e$	$\rightarrow$	$CH + H_2 + H_2$	$8.40 \times 10^{-9}(T/300)^{-0.52}$
R154	$HCO^+ + e$	$\rightarrow$	$CO + H$	$2.40 \times 10^{-7}(T/300)^{-0.69}$
R155	$HOC^+ + e$	$\rightarrow$	$CO + H$	$1.10 \times 10^{-7}(T/300)^{-1.00}$
R156	$OH^+ + e$	$\rightarrow$	$O + H$	$3.75 \times 10^{-8}(T/300)^{-0.50}$
R157	$CO^+ + e$	$\rightarrow$	$C + O$	$2.00 \times 10^{-7}(T/300)^{-0.48}$

Ref. McElroy et al. (2013)

2.4 Radiative heating processes

According to observations of solar-type G stars, the younger the star, the larger the stellar X-ray and EUV luminosities (Ribas et al., 2005). For example, when the stellar age is 100 Myr, the EUV flux is ~ 100 times that of the present Sun. For very young age $\leq 100\,\mathrm{Myr}$, the XUV fluxes may be almost saturated (Lammer et al., 2013; Erkaev et al., 2014). In our model, we apply the XUV spectrum 100 Myr after the birth of the Sun from 0.1 to 165 nm provided by Claire et al. (2012), whose total flux is $6.8 \times 10^2\,\mathrm{ergs\,cm^{-2}\,s^{-1}}$ at the orbit of Earth. Most previous studies cut off UV at 100 nm or 120 nm (e.g. Lammer et al., 2014). But, this study extends the considering UV wavelength because CH_4 absorbs UV above 120 nm. We neglect UV above 165 nm because H_2O that is the main absorber of UV at such wavelength is depleted in the upper atmosphere owing to the effect of cold trap in the troposphere.

In order to calculate the heating rate profile and photolysis rate profiles, the radiative transfer of parallel solar XUV beams in spherically symmetric atmosphere is calculated by applying the method formulated by Tian et al. (2005a). As shown in figure 2, solar

XUV beam penetrates the atmosphere and it is absorbed by Beer's law as follows:

$$F_{\rm XUV}(s, D, \lambda) = F_{\rm XUV}(s + \Delta s, D, \lambda) \exp\left(- \sum_i n_i(r) \sigma^a_{\lambda,i} \Delta s \right), \tag{2.14}$$

where s is the path length, D is the distance from the planetary center to the solar radiation beam, $n_i(r)$ is the number density of species i at r and $\sigma^a_{\lambda,i}$ is the absorption cross section of species i at λ. The energy deposition in a given layer along each path is then multiplied with the area of the ring $2\pi D \Delta D$ to obtain the total energy deposited into the shell segment. The heating rate $q_{\rm abs}(r)$ is given by the total energy absorbed by each shell $E_{\rm shell}(r)$ divided by the volume of the shell $V_{\rm shell}(r)$:

$$q_{\rm abs}(r) = \frac{E_{\rm shell}(r)}{V_{\rm shell}(r)}. \tag{2.15}$$

The photo-absorption cross sections are provided by "PHoto Ionization/Dissociation RATES" (`http://phidrates.space.swri.edu`).

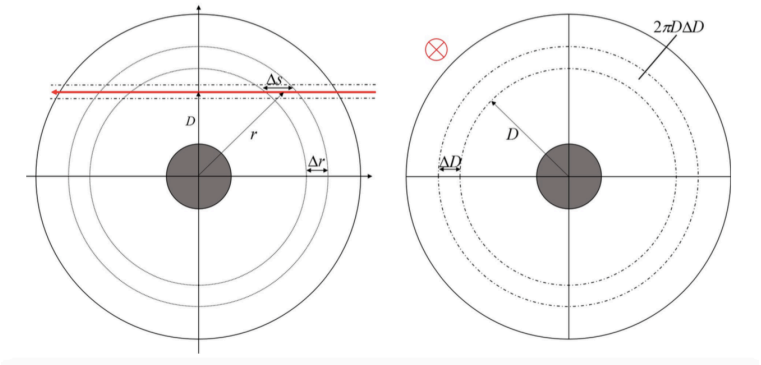

Figure 2.1: Schematic of the two-dimensional energy deposition calculation method. (left) Solar beam is in the plane of the figure. (right) Solar beam is perpendicular to the surface of the paper.

2.5 Radiative cooling processes

We consider radiative cooling by thermal line emissions of CH_4, CO, CH, CH_3 and H_3^+. We calculate the radiative cooling rate $q_{\rm rad}$ by using the photon escape probability

which represents the probability that the emitted photon can escape from the atmosphere without being absorbed or scattered (Castor, 2004). The radiative cooling rate due to a transition from an energy level i to another level j of a radiatively active molecular species s is given by

$$q_{\mathrm{rad},s,ij} = n_{s,i} A_{ij} h\nu_{ij} \beta_{ij}, \tag{2.16}$$

where $n_{s,i}$ is the population density in the level i, A_{ij} is the spontaneous transition probability, $h\nu_{ij}$ is the energy difference between the level i and level j, and β_{ij} is the photon escape probability. $n_{s,i}$ is calculated under the assumption of LTE

$$n_{s,i} = n_s \frac{g_i}{Z} \exp\left(-\frac{E_i}{k_B T}\right) \tag{2.17}$$

where n_s and Z are the total number density and the partition function of species s, and g_i and E_i are the statistical weight and energy of the level i. The total radiative cooling rate by the species s, $q_{\mathrm{rad},s}$, is calculated by summing the radiative cooling rates by all transitions.

The photon escape probability in the direction $\boldsymbol{l}$ at frequency ν is given by

$$\beta_\nu(\boldsymbol{l}) = \exp(-\tau_\nu(\boldsymbol{l})) \tag{2.18}$$

where $\tau_\nu(\boldsymbol{l})$ is the total optical depth in the direction $\boldsymbol{l}$ from the point of photon emission. For an isolated line with the line profile $\phi(\nu)$, the net photon escape probability is given by

$$\beta(\boldsymbol{l}) = \int_0^\infty \phi(\nu) \beta_\nu(\boldsymbol{l}) d\nu. \tag{2.19}$$

Approximating that the half of photons is emitted outward while another half is emitted downward and absorbed by dense, lower atmospheric layers, the bulk escape probability is evaluated by

$$\beta(r) = \frac{1}{2} \int_0^\infty \phi(\nu, r) \beta_\nu(r) d\nu \tag{2.20}$$

where $\beta_\nu(r)$ is the photon escape probability emitted from the radial distance r to the radial direction at frequency ν

$$\beta_\nu(r) = \exp(-\tau_\nu) = \exp\left[-\int_{r_{\mathrm{top}}}^{r} \alpha_L \phi(\nu, r) ds\right] \tag{2.21}$$

where r_{top} is the radius of outer boundary (top of atmosphere) and α_L is the integrated absorption coefficient given by

$$\alpha_L = \frac{c^2}{8\pi\nu_{ij}^2} n_i A_{ij} \left(\frac{n_j g_i}{n_i g_j} - 1 \right). \tag{2.22}$$

We ignore the effect of scattering. In the thermosphere, line shapes are determined by Doppler-broadening mainly (Liou, 2002). Assuming the doppler profile, $\phi(\nu)$ is given by

$$\phi(\nu, r) = \frac{1}{\sqrt{\pi}\Delta\nu_D} \exp\left[-\frac{1}{(\Delta\nu_D)^2} \left(\nu - \nu_0 - \frac{v(r)}{c}\nu_0 \right)^2 \right] \tag{2.23}$$

where $v(r)$ is the velocity profile of radiative sources and ν_0 is the central frequency of the line profile under no flow. $\Delta\nu_D$ is the doppler width, and it is given by

$$\Delta\nu_D = \frac{v_{\rm th}}{c}\nu_0 \tag{2.24}$$

where $v_{\rm th}$ is the thermal velocity of molecules and given by

$$v_{\rm th} = \sqrt{\frac{3k_B T}{m_s}} \tag{2.25}$$

where m_s is the molecular mass of concerning species s. Net $q_{\rm rad}$ is obtained by sum of contributions by CH_4, CO, CH, CH_3 and H_3^+.

We refer the data needed for calculating the radiative cooling rate like transition frequencies, spontaneous transition probabilities, partition functions, etc. provided by HITRAN database (`http://hitran.org`) and ExoMol database (`http://exomol.com`). We consider 11969 transitions of CH_4, 638 transitions of CO, 656 transitions of CH, 1969 transitions of CH_3 and 5200 transitions of H_3^+ to cover more than the 99% of total energy emission in the temperature range of 100 - 1000 K. CH_2 would be also an important infrared active molecule. However, this study does not consider the radiative cooling by CH_2 because there are no data of CH_2 so far.

2.6 Calculation method and numerical settings

Basic equations are solved by numerical integration about time until the physical quantities settle into steady profiles. These equations can be split into advection phases

and nonadvection phases. We employ the CIP method to solve the advection phases (Yabe and Aoki, 1991) to keep numerical stability and accuracy for hydrodynamic escape simulation (Kuramoto et al., 2013). After solving the advection phases, we solve the nonadvection phases with a finite-difference approach. The nonadvection phases of the energy equation are solved explicitly. The nonadvection phases of the continuity equations are solved with the semi-implicit method. The nonadvection phases of the momentum equations are solved implicitly using the quantities of next time step that are obtained by the integration of the energy equation and the continuity equations. The details in the calculation method are described in Appendix A.

The upper boundary of Mars and Earth are set at $r = 50$ Mars radius (1.70×10^5 km) and at $r = 30$ Earth radius (1.91×10^5 km) respectively. The lower boundary of Mars and Earth are set at $r = 4.39 \times 10^3$ km (the Mars radius + 1000 km) and at $r =$ the Earth radius + 1000 km (7.37×10^3 km) respectively assuming formation of massive proto-atmospheres. The interval was divided into 1000 numerical grids with the grid-to-grid intervals exponentially increasing with r. In each simulation run, the atmospheric density and temperature at the lower boundary are fixed. We assume that only H_2, CH_4 and CO exist at the lower boundary. The number density of H_2 at the lower boundary is set at $10^{19}\,\mathrm{m}^{-3}$ on Mars and Earth. The temperatures at the lower boundary on Mars and Earth are set at 150 K and 200 K respectively approximated by the skin temperature, which is the asymptotic temperature at high altitudes of an upper atmosphere. The number densities of CH_4 and CO are given as parameters in each simulation run. The other physical quantities in the lower and upper boundaries are estimated by linear extrapolations from the calculated domain. As the initial condition, we use the steady profiles of the pure hydrogen atmosphere and add CH_4 and CO whose number density profiles are given by the hydrostatic structure. The initial velocities of CH_4 and CO are set at 10^{-5} m/s.

Chapter 3

Hydrodynamic Escape of a reduced proto-atmosphere on Mars

3.1 Atmospheric composition

For Mars, a hybrid-type atmosphere in which the solar component and the degassed component are mixed is supposed (Saito and Kuramoto, 2018). The solar component is approximated by pure H_2. The degassed component consists of H_2, CH_4 and CO referring to the results of Kuramoto (1997). The CH_4/CO ratio in the degassed component highly depends on equilibration pressure and temperature. Thus, we consider three cases of CH_4/CO ratio in the Martian proto-atmosphere: when only CH_4 exists, when only CO exists, and when CH_4/CO=1. The mixing ratio (CH_4+CO)/H_2 is taken to be a parameter because of the uncertainty in their supply to the proto-Mars.

3.2 Results

3.2.1 Atmospheric profiles

Figures 3.1 show the radial profiles of mean velocity, temperature, number density, radiative heating rate and radiative cooling rate for typical steady state solutions of H_2-

CH_4-CO atmospheres. In each solution, the flow is radially accelerated from near zero velocity to supersonic (figure 3.1(a)). Erkaev et al. (2014) assumed that all of molecules in a modeled Martian proto-atmosphere are dissociated into atoms in the upper atmosphere. In our study, a significant fraction of molecules stays undissociated especially in the lower region (Figure 3.1(c)). Figure 3.2 shows the timescale for photolysis and that for advection which are evaluated as follows:

$$t_{i,\mathrm{photolysis}} = \frac{1}{j_i}, \tag{3.1}$$

$$t_{\mathrm{advection}} = \frac{H}{u}, \tag{3.2}$$

where $t_{i,\mathrm{photolysis}}$ and $t_{\mathrm{advection}}$ are the timescale for photolysis of species i and that for advection respectively, j_i is the total photolysis rate of species i, H is the local scale height of the atmosphere and u is the mean velocity. The timescale for advection is shorter than that for dissociation, which indicates that molecules can stay largely undissociated in escaping flow.

3.2.2 Energy balance

Figure 3.3 represents the energy balance in the subsonic region. The heating efficiency which represents the fraction of net energy deposition as sensible heat relative to the total input of XUV energy is given by

$$\eta = \frac{\int_{r_0}^{r_s}(q_{\mathrm{abs}} - q_{\mathrm{ch}} - q_{\mathrm{rad}})4\pi r^2 dr}{\int_{r_0}^{r_s} q_{\mathrm{abs}} 4\pi r^2 dr}, \tag{3.3}$$

where r_0 and r_s are the radial distance of the lower boundary and that of the transonic point, respectively, and q_{abs}, q_{ch} and q_{rad} are the radiative heating rate by XUV absorption, the rate of net chemical expense of energy, and the radiative cooling rate. In the results of figure 3.3, the heating rate is balanced with the sum of cooling rates, enthalpy and kinetic energy outflow rates and potential energy gain rates with accuracy $\sim$5 % error. The heating efficiency decreases as the mixing ratio of CH_4 and CO increases due to radiative cooling by CH_4 and CO: it becomes one order of magnitude smaller than that of the pure hydrogen atmosphere when (CH_4+CO)/$H_2 \gtrsim 0.05$. This result indicates that

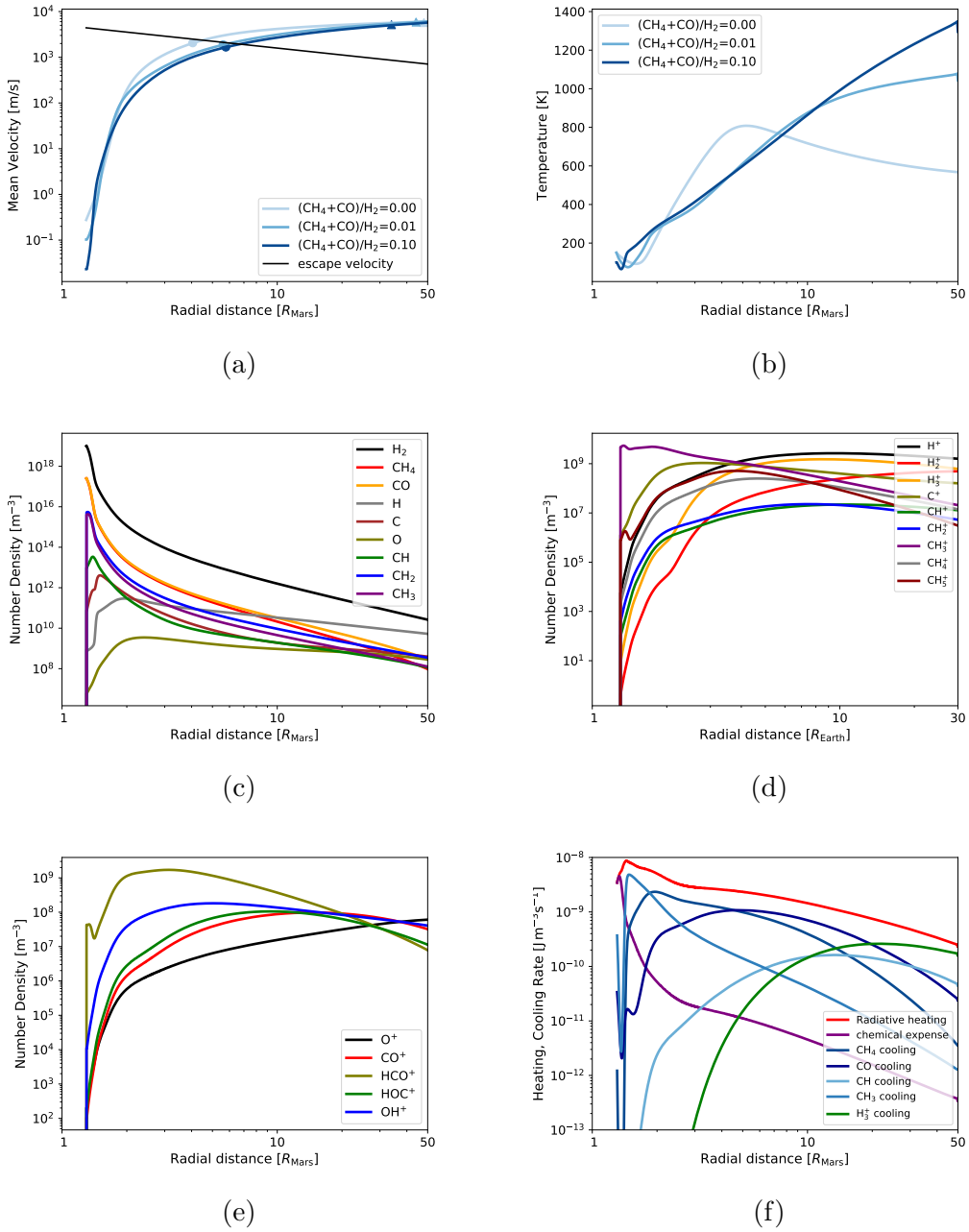

Figure 3.1: Atmospheric profiles. (a) Mean velocity. The dots represent the transonic points and the triangles represent the exobase altitudes. The black line represents the escape velocity. (b) Temperature. (c) Number density of neutral species. (d) (e) Number density of ion species. (f) Radiative heating and radiative cooling rate. The results in (c)–(f) are obtained when CH_4/H_2=CO/H_2 = 0.025.

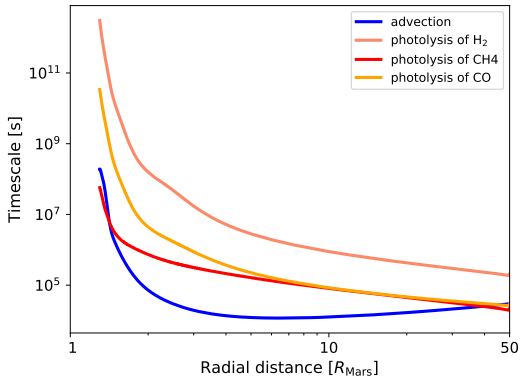

Figure 3.2: Timescale for photolysis and advection when CH_4/H_2=CO/H_2 = 0.025.

the molecular radiative cooling suppresses the atmospheric escape significantly. The decrease in heating efficiency is caused not only the increase in the abundance of coolants but also the increase in temperature. The addition of CH_4 and CO increases the mean molecular weight of the atmosphere. Then, the flow velocity and adiabatic cooling rate decrease even if mass escape flux was kept constant. Indeed, the Lagrangian change of gas temperature is given by

$$\frac{DT}{Dt} = \frac{q}{k_\gamma k_B n} - \frac{T}{k_\gamma}\frac{1}{r^2}\frac{\partial}{\partial r}(ur^2), \tag{3.4}$$

where the second term on the right-hand side of this equation represents the effect of adiabatic cooling. The decrease in adiabatic cooling rate results in the temperature increase in the subsonic region, which acts to enhance the radiative cooling.

Figure 3.4 represents the heating efficiencies on H_2-CH_4 atmospheres, H_2-CO atmospheres, and H_2-CH_4-CO atmospheres, which indicates that the decreasing trend of heating efficiency becomes large as the CH_4/CO ratio increases. This is because CH_4 is more radiatively active than CO in the temperature region of the Martian atmosphere than CO (figure 3.5).

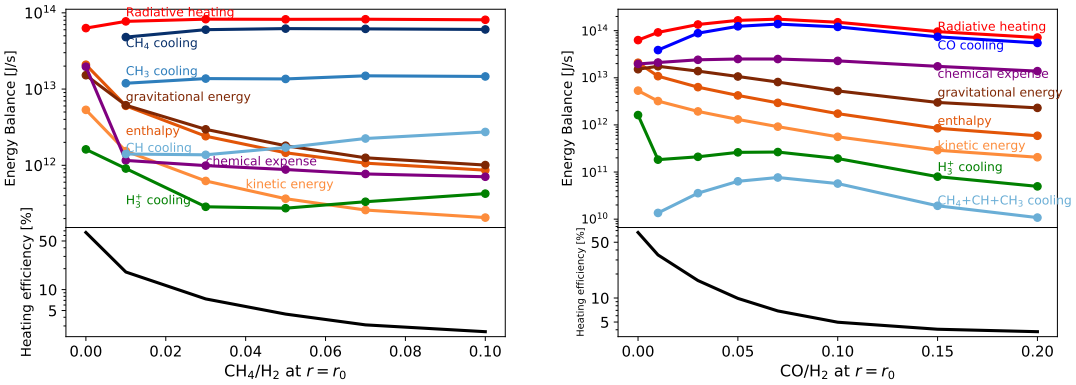

(a)

(b)

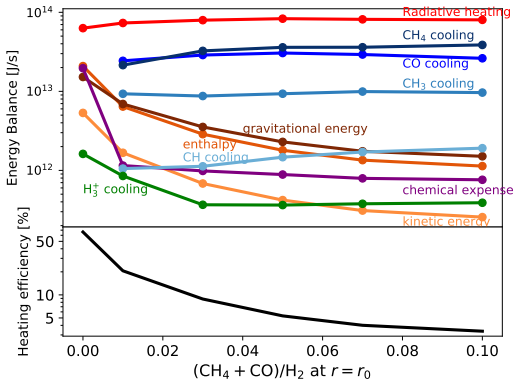

(c)

Figure 3.3: Energy balance in the subsonic region. (a) Energy balance on H_2-CH_4 atmospheres. (b) Energy balance on H_2-CO atmospheres. (c) Energy balance on H_2-CH_4-CO atmospheres.

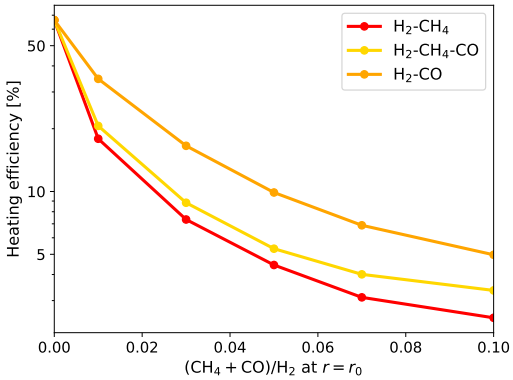

Figure 3.4: Heating efficiency in the subsonic region. The red line represent the heating efficiency on H_2-CH_4 atmospheres, the orange line represents that on H_2-CO atmospheres, and the yellow line represents that on H_2-CH_4-CO atmospheres.

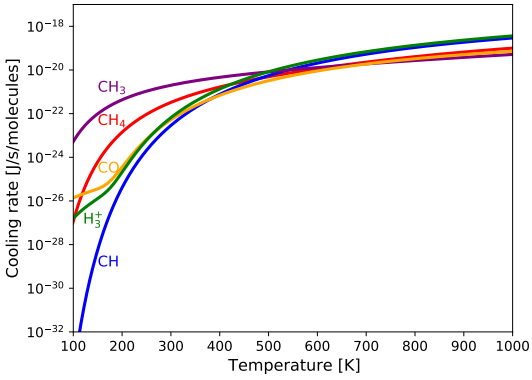

Figure 3.5: Radiative cooling rate per one molecule as a function of temperature.

3.2.3 Escape rate and mass fractionation

Figure 3.6 represents the relationship between the total escape mass fluxes and the lower boundary mixing ratio (CH_4+CO)/H_2. Here, the bulk escape molecular fluxes of H_2, CH_4 and CO are given by

$$F_i = 4\pi r_0^2 n_i(r_0) v_i(r_0), \tag{3.5}$$

where $i = H_2, CH_4$ and CO, respectively. Note that the dissociation of these species are negligible at the lowest region near $r = r_0$. The total escape mass flux $F_{\rm mass}^{\rm total}$ is given by

$$F_{\rm mass}^{\rm total} = \sum_i m_i F_i, \tag{3.6}$$

where m_i is the molecular mass of species i (H_2, CH_4 and CO). As the basal mixing ratios of CH_4 and CO increase, the escape mass flux decreases due to the radiative cooling by CH_4 and CO (figure 3.3 and 3.4). The decreasing trend of the escape mass flux becomes large as the basal CH_4/CO ratio increases due to the more effective radiative cooling of CH_4.

Figure 3.7 represents the relationship between the basal CH_4/H_2 (CO/H_2) ratio and the fractionation factor ($= (F_i/F_{H_2})/(n_i(r_0)/n_{H_2}(r_0)) = v_i(r_0)/v_{H_2}(r_0)$) which represents the degree of the mass fractionation. As the mixing ratios increase, the mass fractionation between H_2 and CH_4 (or CO) occurs more remarkably. This result indicates that more fraction of CH_4 and CO tend to be left behind as they become more dominant in the proto-atmosphere. The fractionation factor can be represented by using the crossover mass m_c, the largest molecular mass of secondary constituent that can be dragged upward to space by the dominant lighter gas, which is given by

$$m_c = m_{H_2} + \frac{kTF_{H_2}}{b_{H_2,i} g X_{H_2}} \tag{3.7}$$

where m_{H_2}, F_{H_2} and X_{H_2} are the molecular mass, number flux and mixing fraction of H_2 and $b_{H_2,i}$ is the binary diffusion coefficient between H_2 and species i (Hunten et al., 1987). The relative escape flux of the secondary constituent with molecular mass m_i

follows (Hunten et al., 1987)

$$\frac{F_i/F_{\mathrm{H_2}}}{n_i(r_0)/n_{\mathrm{H_2}}(r_0)} = \frac{m_c - m_i}{m_c - m_{\mathrm{H_2}}}. \tag{3.8}$$

The dashed lines of figure 3.7 are obtained from the equation (3.8), which approximately explain the numerical results represented by solid lines. The slight deviation from analytical formula may be caused by effects of photolysis which affects the molecular masses and hydrogen mixing ratio.

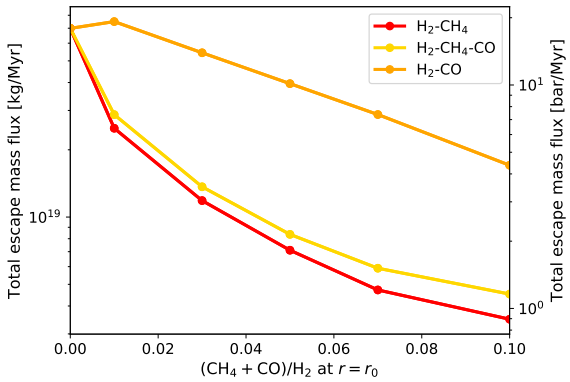

Figure 3.6: Escape mass fluxes of main species per 1 Myr as a function of the lower boundary mixing ratio (CH_4+CO)/H_2.

3.2.4 Effect of change in XUV flux

Although we have assumed the solar XUV flux 100 times the present, there remains significant uncertainty in the XUV flux of the early Sun (Tu et al., 2015). Thus, we also conduct simulations with the XUV flux 50 times and 200 times as large as the present. Figure 3.8 represents the atmospheric escape rates normalized by the values when the XUV flux is 100 times the present. The atmospheric escape rate on H_2-CO atmosphere approximately obeys the energy-limited relation for different XUV flux (figure 3.8(a)). On the other hand, the atmospheric escape rate on H_2-CH_4 atmosphere does not increase proportionally with the XUV flux simply, but the increasing trend in the escape rate

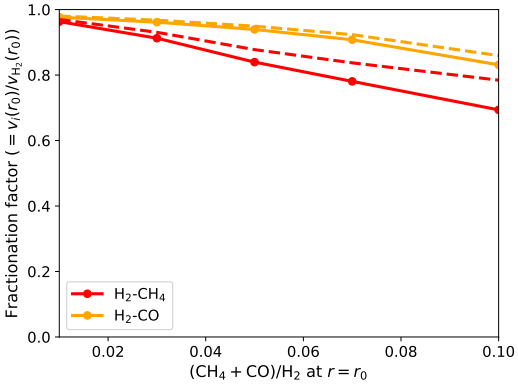

Figure 3.7: Fractionation factors as a function of the lower boundary mixing ratio $(CH_4+CO)/H_2$.

weakens as the XUV flux and the CH_4/H_2 ratio increase (figure 3.8(b)). This is because the heating efficiency decreases due to the increase in the production of CH and CH_3.

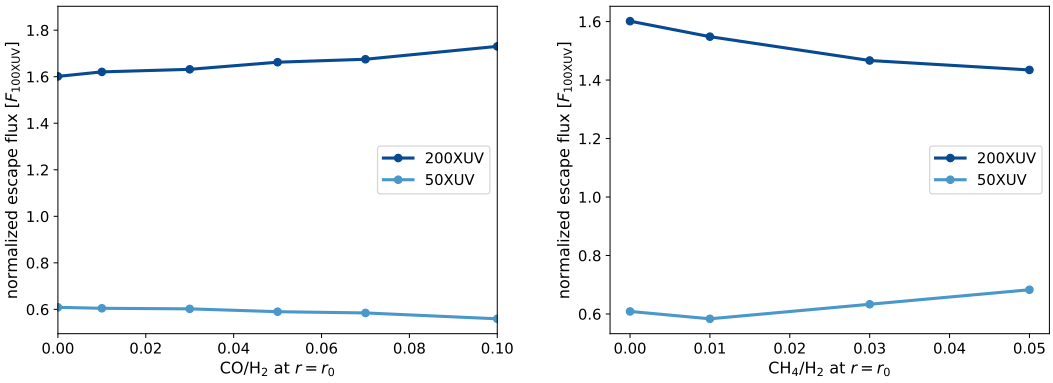

(a) (b)

Figure 3.8: Escape rates normalized by the standard value. (a) Escape rates on H_2-CH_4 atmospheres. (b) Escape rates on H_2-CO atmospheres.

3.3 Discussion

3.3.1 Evolution of early Martian atmosphere

Possible changes in the amount of early Martian atmosphere

The evolution of the Martian proto-atmosphere which is consistent with the current inventory of Martian volatiles can be estimated from our numerical results. The lower limit of integrated CO_2 loss to space from 4.2 Ga to the present estimated from observations by MAVEN spacecraft is 0.8 bar (Jakosky et al., 2018). Therefore, about 1 bar of carbon species was likely left when most H_2 lost to space via hydrodynamic escape. As the standard setting, we suppose that a CH_4 (or CO) atmosphere whose total amount of carbon is equivalent to that of 1 bar of CO_2 was left behind after H_2 loss. In addition, the XUV flux is kept constant at 100 times the present.

We use the escape flux and the fractionation factor in section 3.2.3 to describe the change in atmospheric amount. Referring to figure 3.7, the fractionation factors $(F_{CH_4}/F_{H_2})/(n_{CH_4}(r_0)/n_{H_2}(r_0))$ and $(F_{CO}/F_{H_2})/(n_{CO}(r_0)/n_{H_2}(r_0))$ is approximated by the following fitting function:

$$\frac{F_i/F_{H_2}}{n_i(r_0)/n_{H_2}(r_0)} = \frac{1}{1+af}, \tag{3.9}$$

where a is the fitting factor and $f = n_i(r_0)/n_{H_2}(r_0)$ (i =CH_4, CO). We define N_i as the total molecular number of species i in the atmosphere. Using equation (3.9), $F_i = -dN_i/dt$ and $n_i(r_0)/n_{H_2}(r_0) \simeq N_i/N_{H_2}$,

$$N_i(f) = N_i^0 \exp\left[-\frac{1}{a}\left(\frac{1}{f^0} - \frac{1}{f}\right)\right]. \tag{3.10}$$

where N_i^0 and f^0 are the initial total molecular number of species i and the initial N_i/N_{H_2} ratio, respectively. The CH_4 line and CO line of figure 3.7 can be fitted by $a = 4.05$, 3.17 respectively. Assuming that the hydrodynamic escape stops when $f = f^t$, N_i^0 is given by

$$N_i^0 = N_i^t \exp\left[\frac{1}{a}\left(\frac{1}{f^0} - \frac{1}{f^t}\right)\right]. \tag{3.11}$$

where N_i^t is the value when $f = f^t$. Here we assume that $f^t = 1, 0.67$ on H_2-CH_4 atmosphere and H_2-CO atmosphere respectively, when the crossover mass reaches the mass of CH_4 and CO. Note that changes in the assumption for the terminal f value little affect the estimate of initial abundance N_i^0. Accordingly, the atmospheric masses with f are given by

$$M_i(f) = m_i N_i(f), \tag{3.12}$$

$$M_{\mathrm{H_2}}(f) = m_{\mathrm{H_2}} N_{\mathrm{H_2}}(f) = m_{\mathrm{H_2}} \frac{N_i(f)}{f}, \tag{3.13}$$

where m_i is the molecular mass of species i. On the other hand, the temporal change of f follows

$$\frac{df}{dt} = \frac{a f^2 F_i(f)}{N_i(f^0) \exp\left[-\frac{1}{a}\left(\frac{1}{f^0} - \frac{1}{f}\right)\right]}. \tag{3.14}$$

Given the initial $N_i/N_{\mathrm{H_2}}$ ratio and the escape flux F_i following figure 3.5, the change in the amount of atmosphere over time is obtained from equations (3.12), (3.13) and (3.14).

Figures 3.9 represent the temporal change in the equivalent surface pressure when the initial amount of H_2 is equivalent to the maximum amount of the nebula envelope estimated by Erkaev et al. (2014). Here the equivalent surface pressure is given by

$$P_i = \frac{M_i g}{4\pi R_p^2}, \tag{3.15}$$

where P_i is the surface pressure of species i, M_i is the atmospheric mass of species i, g is the gravitational acceleration, and R_p is the radius of Mars. The amounts of CH_4 and CO lost by hydrodynamic escape are as much as ~ 10 bar equivalent to ~ 25 bar of CO_2 and ~ 20 bar equivalent to ~ 30 bar of CO_2, respectively. If Mars accreted carbon with a proportion similar to those of Earth and Venus which currently have CO_2 equivalent ~ 100 bar on their surfaces, Mars should have gained carbon equivalent to ~ 15 bar of CO_2 considering the differences of the planetary mass, surface area and gravity. The hydrodynamic escape of hydrogen-rich proto-atmosphere in which the degassed component and solar component are mixed may largely explain the paucity of CO_2 on present Mars compared to Earth and Venus.

Figures 3.10 represent the dependence of the initial atmospheric amounts on the initial CH_4/H_2 (CO/H_2) ratio. The initial atmospheric amount and the total amount lost by hydrodynamic escape decreases as the initial mixing ratio of carbon species increases. CH_4 and CO can hardly escape when the mixing ratios of CH_4 and CO is larger than ~ 0.5.

Figure 3.11 represents the dependence of the timescale for H_2 escape on the initial amount of H_2. Atmospheres including CH_4 and CO have longer timescale than the pure hydrogen atmosphere due to the effect of their radiative cooling and higher mean molecular weight in the atmospheres. The timescale reaches ~ 10 Myr when the initial amount of H_2 is the maximum of the nebula envelope estimated by Erkaev et al. (2014). The initial amount of H_2 may have been larger than the estimation by Erkaev et al. (2014) because the hybrid-type atmosphere could contain more nebula gas component due to the higher mean molecular weight. Moreover, a large amount of hydrogen may have been supplied from the degassed component. Due to its large distance from the Sun, Mars was likely formed from volatile-rich building blocks that had been prepared under cold nebular environments (Dreibus and Wanke, 1985). When employing the two-component model for Martian building blocks described by Dreibus and Wanke (1987) and considering the reduction of the degassed component by metallic iron, ~ 100 bar of H_2 is estimated to be formed (Saito and Kuramoto, 2018). Thus, the timescale for H_2 escape may have been longer than ~ 100 Myr.

Recently, organic matters are detected from ~ 3.5 Ga mudstones in Gale crater (e.g. Eigenbrode et al., 2018) and ~ 4 Ga carbonates in Martian meteorite, Allan Hills 84001 (Koike et al., 2020), which indicates that early Mars had a reduced environment suitable for the production of organic matters. Our result that a hydrogen-rich reduced environment may have been kept for a period order of 100 Myr seems consistent with these detections of organic matters derived from early Mars.

Isotopic fractionation in early Martian atmosphere during hydrodynamic escape

Our escape model is applicable to isotopic fractionation of hydrogen, carbon, and oxygen during hydrodynamic escape. From equations (3.7), (3.8), $F_i = -dN_i/dt$ and $n_i(r_0)/n_{\mathrm{H_2}}(r_0) \simeq N_i/N_{\mathrm{H_2}}$, changes in atmospheric amount of minor components are given by

$$\frac{N_i}{N_i^0} = \exp\left(\int_{N_{\mathrm{H_2}}^0}^{N_{\mathrm{H_2}}} \frac{m_c - m_i}{m_c - m_{\mathrm{H_2}}} \frac{1}{N_{\mathrm{H_2}}} dN_{\mathrm{H_2}}\right). \tag{3.16}$$

where N_i and N_i^0 are the total molecular number of species i and its initial value respectively. Using this equation and atmospheric evolutionary track of H_2, the change in the isotopic compositions can be calculated. The $^{13}C/^{12}C$ ratio, $^{15}N/^{14}N$ ratio, D/H ratio, $^{22}Ne/^{20}Ne$ ratio, $^{38}Ar/^{36}Ar$ ratio, and $^{131}Xe/^{130}Xe$ ratio are given by

$$\frac{^{13}\mathrm{C}}{^{12}\mathrm{C}} = \begin{cases} \frac{N_{^{13}\mathrm{CH_4}}}{N_{^{12}\mathrm{CH_4}}} \\ \frac{N_{^{13}\mathrm{CO}}}{N_{^{12}\mathrm{CO}}} \end{cases} \tag{3.17}$$

$$\frac{^{15}\mathrm{N}}{^{14}\mathrm{N}} = \begin{cases} \frac{N_{^{15}\mathrm{NH_3}}}{N_{^{14}\mathrm{NH_3}}} \\ \frac{N_{^{15}\mathrm{N}^{14}\mathrm{N}}}{2N_{^{14}\mathrm{N_2}} + N_{^{15}\mathrm{N}^{14}\mathrm{N}}} \simeq \frac{N_{^{15}\mathrm{N}^{14}\mathrm{N}}}{2N_{^{14}\mathrm{N_2}}} \end{cases} \tag{3.18}$$

$$\left(\frac{\mathrm{D}}{\mathrm{H}}\right)_{\mathrm{atomsphere}} = \frac{N_{\mathrm{HD}}}{2N_{\mathrm{H_2}} + N_{\mathrm{HD}}} \simeq \frac{N_{\mathrm{HD}}}{2N_{\mathrm{H_2}}}, \tag{3.19}$$

$$\left(\frac{\mathrm{D}}{\mathrm{H}}\right)_{\mathrm{ocean}} = \frac{N_{\mathrm{HDO}}}{2N_{\mathrm{H_2O}} + N_{\mathrm{HDO}}} \simeq \frac{N_{\mathrm{HDO}}}{2N_{\mathrm{H_2O}}}, \tag{3.20}$$

$$\frac{^{22}\mathrm{Ne}}{^{20}\mathrm{Ne}} = \frac{N_{^{22}\mathrm{Ne}}}{N_{^{20}\mathrm{Ne}}}, \tag{3.21}$$

$$\frac{^{38}\mathrm{Ar}}{^{36}\mathrm{Ar}} = \frac{N_{^{38}\mathrm{Ar}}}{N_{^{36}\mathrm{Ar}}}, \tag{3.22}$$

$$\frac{^{131}\mathrm{Xe}}{^{130}\mathrm{Xe}} = \frac{N_{^{131}\mathrm{Xe}}}{N_{^{130}\mathrm{Xe}}}. \tag{3.23}$$

It is unknown what is the main nitrogen species in the proto-atmosphere, thus we consider two cases: when N_2 is the main species and when NH_3 is the main species in the proto-atmosphere.

We calculate the atmospheric D/H ratio and ocean D/H ratio respectively. We assume that the following deuterium exchange reaction occurs and it always equilibrates referring to Genda and Ikoma (2008):

$$\mathrm{HD} + \mathrm{H_2O} \leftrightarrow \mathrm{HDO} + \mathrm{H_2}. \tag{3.24}$$

The equilibrium constant for this reaction is given by

$$K \simeq \frac{(\mathrm{D/H})_{\mathrm{ocean}}}{(\mathrm{D/H})_{\mathrm{atmosphere}}} = \frac{0.22 \times 10^6}{T^2} + 1 \tag{3.25}$$

where T is the temperature (Richet et al., 1977; Genda and Ikoma, 2008). The amount of ocean on early Mars is highly uncertain. We assume that the amount of the seawater is constant at 0.1 times the present amount of the Earth's ocean and the surface temperature is 300 K constantly.

Figures 3.12 represent the ratios of final isotopic compositions when $f = f_t$ to the initial isotopic compositions of H, C, and N with the initial amount of H_2, and Figures 3.13 represent the ratios of final isotopic compositions when $f = f_t$ to the initial isotopic compositions of noble gases. The D/H ratio increases at most by a factor of 3.5 due to the isotopic fractionation by hydrodynamic escape and the deuterium concentration via the deuterium exchange reaction between ocean and atmosphere (figure 3.12(a)). If the hybrid-type atmosphere was formed, the D/H ratio may have been between the value of the solar nebula and that of the degassed component. The D/H ratio of the degassed component was likely close to those of primitive meteorites and that of the present Earth's seawater which is about 6 times larger than that of solar nebula gas (Marty, 2012). On the other hand, atmospheric water vapor on Mars has a D/H ratio of ∼6-7 times higher than that of the terrestrial seawater (e.g. Krasnopolsky, 2000; Villanueva et al., 2015). ALH84001 meteorite with crystalline age at 4.1 Ga contains trapped water with D/H ratio ∼1.5-2 times higher than that of the terrestrial seawater (Usui et al., 2012), suggesting that the D/H fractionation had already proceeded. Our result may consistent with the high D/H ratio of the ALH84001 meteorite.

$(^{13}\mathrm{C}/^{12}\mathrm{C})_{\mathrm{final}}/(^{13}\mathrm{C}/^{12}\mathrm{C})_{\mathrm{initial}}$ is at most ~ 1.2 (figure 3.12(b)). The $^{13}\mathrm{C}/^{12}\mathrm{C}$ ratio of the present Martian CO_2 atmosphere is higher by a factor of 1.05 than that of Earth and

primitive meteorites (Henderson and Henderson, 2009; Lodders, 2010b). The $^{13}C/^{12}C$ ratio of carbonates in ALH84001 is higher by a factor of 1.04 than that of Earth (Nile et al., 2013), which suggests that carbon was mostly fractionated in the early era (Catling and Kasting, 2017). If the initial $^{13}C/^{12}C$ ratio of Mars is similar to that of Earth and primitive meteorites, isotopic fractionation of carbon by the hydrodynamic escape of proto-atmosphere can explain the $^{13}C/^{12}C$ ratios of present Mars and ALH84001. The final $^{13}C/^{12}C$ ratios starting from the massive hydrogen-rich atmospheres seems slightly too high. However, cases with such efficient $^{13}C/^{12}C$ fractionation by hydrodynamic escape may be compatible with the observed weak isotopic fractionation because the late supply of carbon species by mantle degassing and meteoroid bombardments to the early atmosphere likely dilutes the isotopic fractionation.

The isotopic fractionations of nitrogen and noble gases by hydrodynamic escape are also simulated (figure 3.12(c)(d); figure 3.13), but it is shown that the strong fractionation suggested from the present isotopic ratios cannot be explained by the hydrodynamic escape alone. Non-thermal escape processes such as solar-wind-induced sputtering and photochemical escape also likely have fractionated nitrogen, Ne, and Ar (Jakosky et al., 1994). Considering the effect of non-thermal escape additionally, the present isotopic composition of nitrogen, Ne, and Ar could be explained.

Effect of weakly constrained parameters on estimated atmospheric evolution

To estimate the evolution of the proto-atmosphere, we adopted nominal values for the weakly constrained parameters such as the XUV flux and the atmospheric mass lost by processes except for hydrodynamic escape. Here we consider the effects of ambiguity in these constraints on the estimated atmospheric evolution.

XUV flux There remains significant uncertainty in the XUV flux of the early Sun (Tu et al., 2015). If the XUV flux and escape flux change, the atmospheric evolutionary track likely change. Here we consider the atmospheric evolution when the XUV flux differs, the atmospheric evolutionary track likely changes associated with escape rate.

Figure 3.14 represents the timescale for H_2 escape when the XUV flux is twice as large as the standard-setting. Here CH_4 or CO equivalent to 1 bar of CO_2 is assumed to be left behind after the completion of hydrodynamic escape for each initial amount of H_2. The timescale becomes shorter slightly when the XUV flux becomes higher, but not proportional to the XUV flux because the CH_4/H_2 (CO/H_2) ratio becomes larger when the initial atmospheric amounts is the same under the standard-setting. The degree of isotopic fractionation becomes large slightly as the XUV flux becomes higher (figures 3.15 and 3.16).

Atmospheric mass after hydrodynamic escape We assume that a CH_4 (or CO) atmosphere whose total amount of carbon is equivalent to that of 1 bar of CO_2 was left behind after hydrodynamic escape of H_2 referring to the estimation of the atmospheric amount lost by non-thermal escape flux by MAVEN spacecraft. However, Mars may have other carbon inventories such as carbonates in the subsurface. Carbonates are found in martian soil, which contains 3-5 wt% magnesite ($MgCO_3$) at the Mars Phoenix landing site (e.g. Boynton et al., 2009). If this mass fraction were representative of the crust down to 1 km, then about 1 bars of CO_2 could be sequestered (Catling and Kasting, 2017). If the remaining atmospheric amount increases considering deposition of carbon additionally, the estimated initial atmospheric amount and the timescale for H_2 increase almost proportionally.

3.3.2 Preservation of atmospheres on proto-planets

The mass of Mars is consistent with the predicted mass of proto-planets formed by the oligarchic growth of planetesimals in the solar nebula (Kokubo and Ida, 1998). The Earth, about ten times more massive than Mars, is considered to be formed through the collision of proto-planets over several tens Myr mostly after the dissipation of the solar nebula. During the giant impact stage, the hydrodynamic escape of the proto-atmosphere is expected to occur from each proto-planet. Here we apply our escape modeling to explore how much proto-atmosphere would remain on proto-planets before merge into a larger

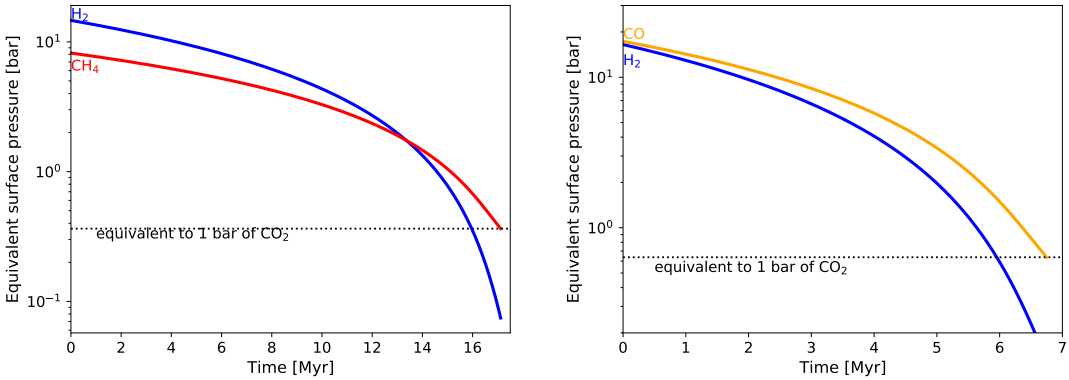

(a) (b)

Figure 3.9: Changes in the equivalent surface pressure over time when the initial amount of H_2 is equivalent to the maximum amount of the nebula envelope estimated by Erkaev et al. (2014). (a) Changes in the amount of a H_2-CH_4 atmosphere. (b) Changes in the amount of a H_2-CO atmosphere.

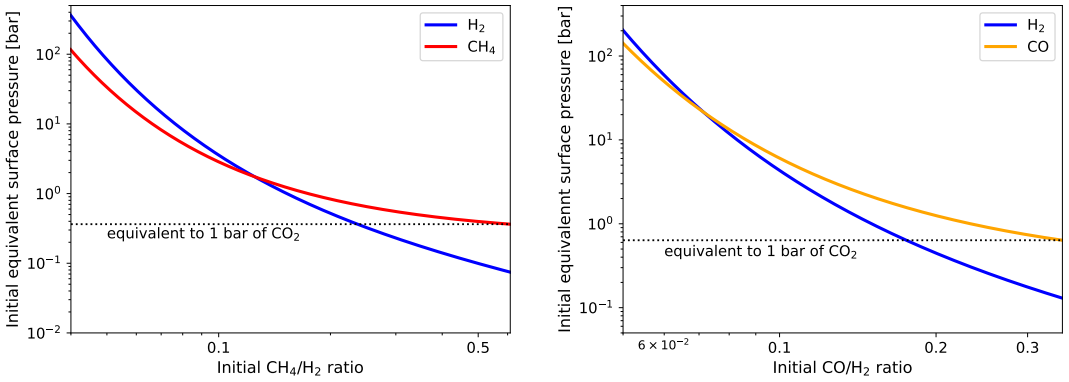

(a) (b)

Figure 3.10: Initial atmospheric amounts with initial CH_4/H_2 (CO/H_2) ratios. (a) Initial atmospheric amounts of H_2-CH_4 atmospheres. (b) Initial atmospheric amounts of H_2-CO atmospheres.

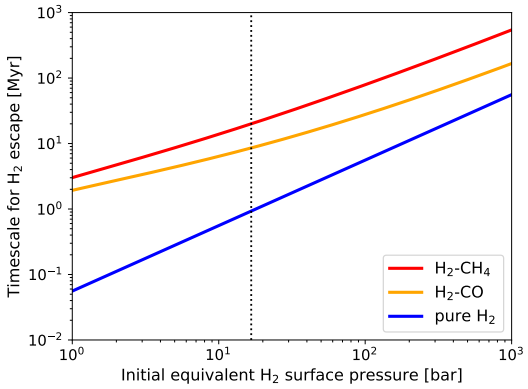

Figure 3.11: Timescale for H_2 escape with the initial amount of H_2. The red line, orange line, and blue line represent the timescale for H_2 escape on H_2-CH_4 atmospheres, H_2-CO atmospheres, and pure H_2 atmospheres.

planet.

Figures 3.17 represent the ratios of the remaining atmospheric amounts to the initial atmospheric amounts assuming that hydrodynamic escape continues 10 Myr under the XUV flux 100 times the present. This indicates that part of the hydrogen-rich atmospheres on Mars-sized proto-planets would remain when the mixing ratios of carbon species are high. Odert et al. (2018) suggested that H_2O-CO_2 steam atmospheres on proto-planets were lost efficiently via hydrodynamic escape and proto-planets in the terrestrial planetary region became volatile-poor. In contrast, our result implies that atmospheres on proto-planets may have survived considerably, and merge into the proto-atmosphere of the larger terrestrial planets such as Earth. Note that the giant impact process itself is also difficult to remove the entire atmospheric mass to space (Genda and Abe, 2005).

3.4 Conclusion

Here we carry out our one-dimensional hydrodynamic escape simulation for Martian proto-atmospheres originated from the degassed component and the solar nebula com-

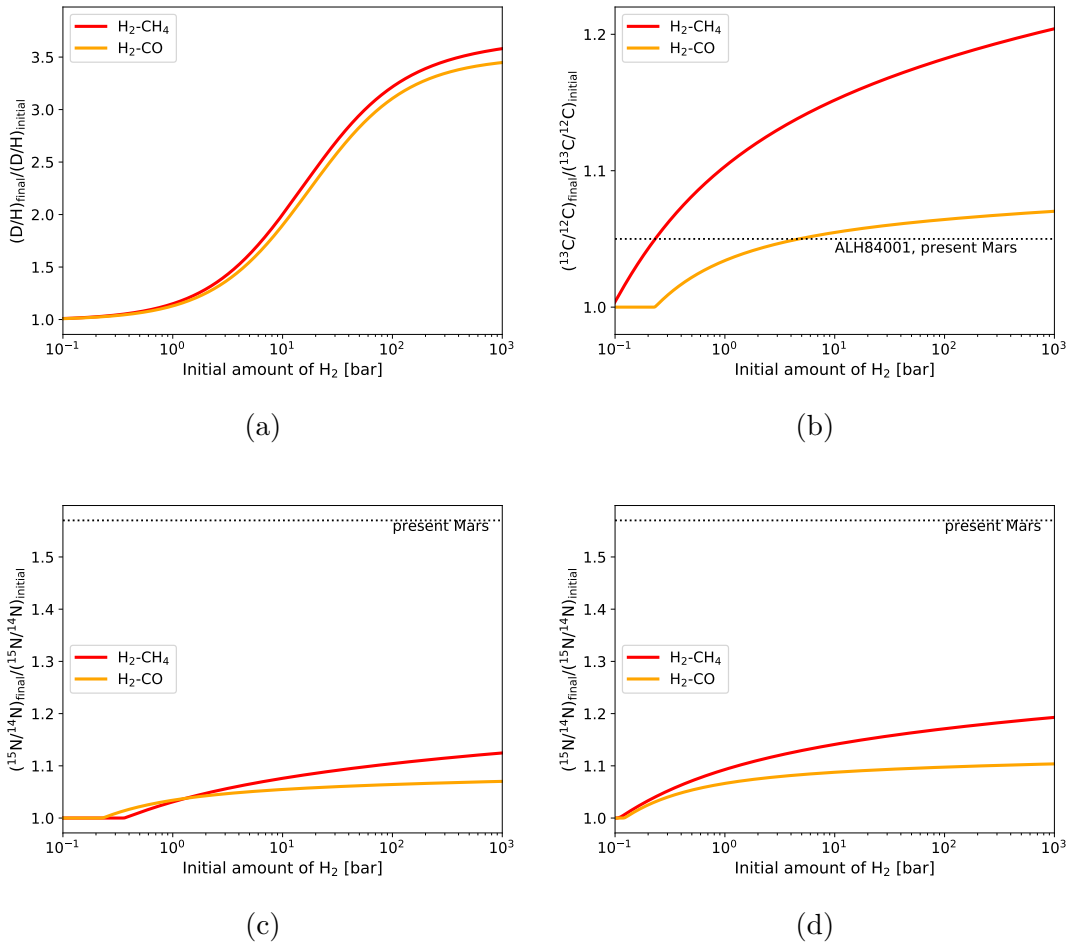

Figure 3.12: Ratio of final isotopic compositions when $f = f_t$ to initial isotopic compositions with initial amounts of H_2. The red lines show isotopic compositions along the atmospheric evolution of H_2-CH_4 atmospheres, and the orange lines show isotopic compositions along the atmospheric evolution of H_2-CO atmospheres. We assume that the initial isotopic compositions of carbon and nitrogen are equal to those of Earth, which are very close to those of primitive meteorites. (a) Ratios of final D/H ratios to initial D/H ratios of the entire system. (b) Ratios of final $^{13}C/^{12}C$ ratios to initial $^{13}C/^{12}C$ ratios. $^{13}C/^{12}C = N_{^{13}CH_4}/N_{^{12}CH_4}$ and $^{13}C/^{12}C = N_{^{13}CO}/N_{^{12}CO}$ are assumed on the red line and on the orange line, respectively. (c) Ratios of final $^{15}N/^{14}N$ ratios to initial $^{15}N/^{14}N$ ratios. Here we assume that $^{15}N/^{14}N = N_{^{15}N^{14}N}/2N_{^{14}N_2}$. (d) Ratios of final $^{15}N/^{14}N$ ratios to initial $^{15}N/^{14}N$ ratios. Here we assume that $^{15}N/^{14}N = N_{^{15}NH_3}/N_{^{14}NH_3}$.

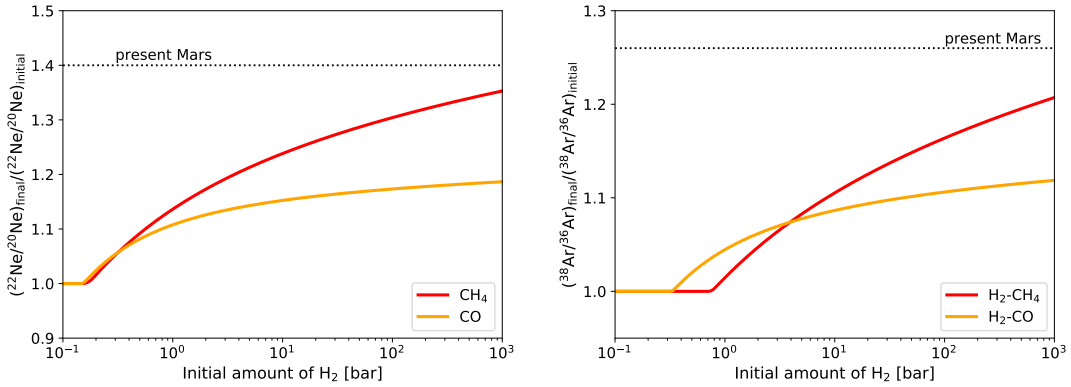

Figure 3.13: Ratios of final isotopic compositions when $f = f_t$ to initial isotopic compositions with initial amounts of H_2. The red lines show isotopic compositions along the atmospheric evolution of H_2-CH_4 atmospheres, and the orange lines show isotopic compositions along the atmospheric evolution of H_2-CO atmospheres. We assume that the initial isotopic compositions are equal to the solar isotopic compositions. (a) Ratios of final $^{22}Ne/^{20}Ne$ ratios to initial $^{22}Ne/^{20}Ne$ ratios. (b) Ratios of final $^{38}Ar/^{36}Ar$ ratios to initial $^{38}Ar/^{36}Ar$ ratios. (c) Rratios of final $^{131}Xe/^{130}Xe$ ratios to initial $^{131}Xe/^{130}Xe$ ratios.

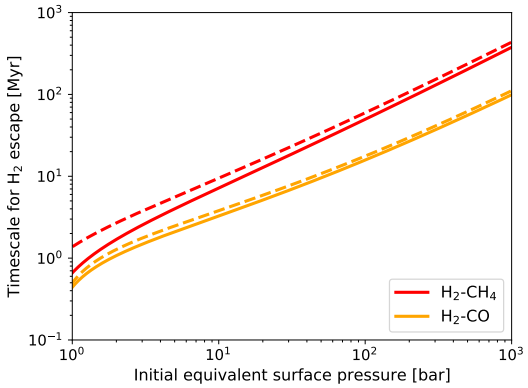

Figure 3.14: Timescale for H_2 escape with initial amounts of H_2. The solid lines represent the timescales when the XUV flux is twice as large as the standard setting, and the dashed lines represent the timescales when the XUV flux is the standard setting.

ponent. According to our results, the atmospheric escape rate decreases more than one order of magnitude and the mass fractionation occurs more remarkably as the mixing ratio of CH_4 and CO increases primarily because of the energy loss by radiative cooling. Assuming 1 bar of CO_2 was left behind when most H_2 completed its hydrodynamic escape, the total amount of carbon species lost by hydrodynamic escape exceeds that equivalent to 20 bar of CO_2 when the proto-Mars obtained $\gtrsim 10$ bar of H_2, which may explain the paucity of CO_2 on Mars compared to Earth and Venus. The timescale for H_2 escape from H_2-CH_4-CO atmospheres becomes longer than that from pure hydrogen atmospheres especially when the CH_4/CO ratio is high. If the proto-Mars obtained > 100 bar of H_2, the timescale for H_2 escape exceeds ~ 100 Myr, which implies that a reduced environment may have been kept on early Mars leaving surface deposition of organic matter produced by atmospheric chemistry under reduced condition. Our result also implies that atmospheres on Mars-sized proto-planets survived during the giant impact phase and involved to the proto-atmophere of larger terrestrial planets like Earth.

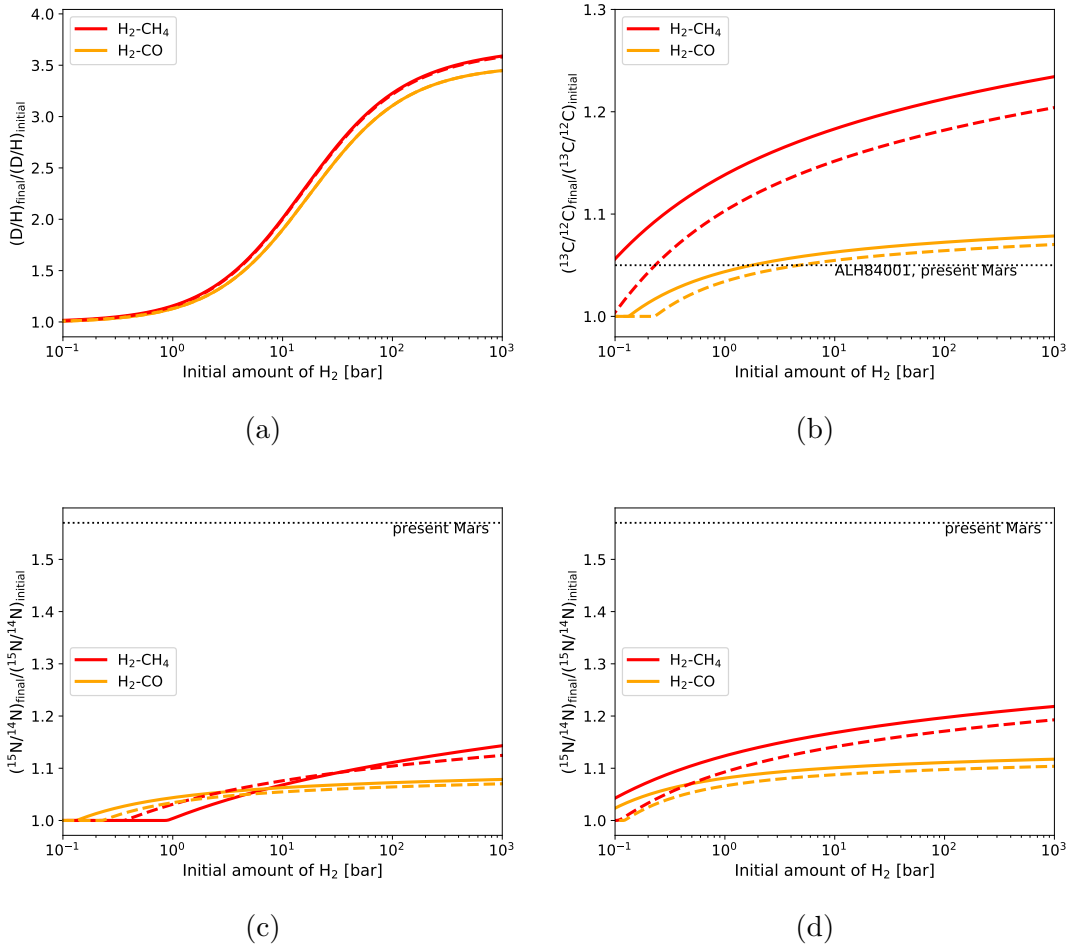

Figure 3.15: Ratios of final isotopic compositions when $f = f_t$ to initial isotopic compositions with initial amounts of H_2. The solid lines represent the timescales when the XUV flux is twice as large as the standard setting, and the dashed lines represent the timescales when the XUV flux is the standard setting. Other line settings are same as figures 3.12.

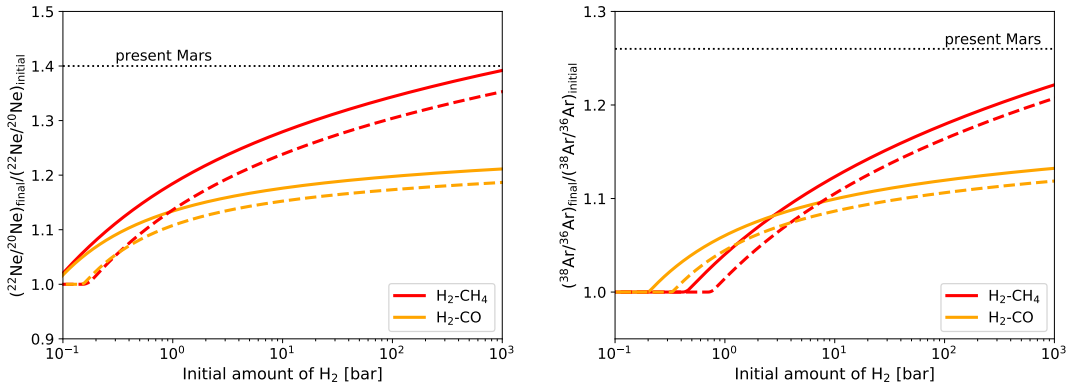

Figure 3.16: Ratios of final isotopic compositions when $f = f_t$ to initial isotopic compositions with initial amounts of H_2. The solid lines represent the timescales when the XUV flux is twice as large as the standard setting, and the dashed lines represent the timescales when the XUV flux is the standard setting. Other line settings are same as figures 3.13.

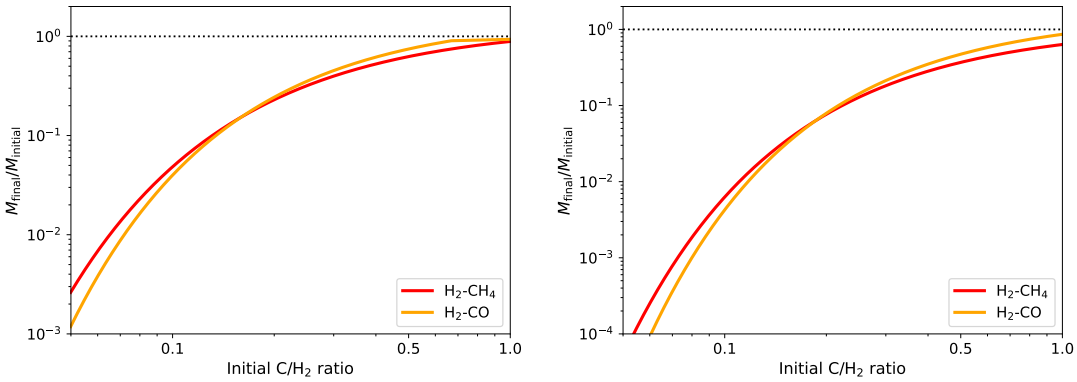

(a) (b)

Figure 3.17: Ratios of remaining atmospheric amounts to initial atmospheric amounts. (a) Ratios when the XUV flux is the standard setting. (b) Ratios when the XUV flux is twice as large as the standard setting.

Chapter 4

Hydrodynamic Escape of a reduced proto-atmosphere on Earth

4.1 Atmospheric composition

Recent studies of isotopic compositions of Earth's materials and primitive meteorites indicate that most of Earth's building blocks were close to enstatite meteorites, which have the most reduced oxidation state among primitive meteorites (Dauphas, 2017). According to the thermodynamic modeling by Kuramoto and Matsui (1996), partitioning of H and C among fluid, silicate melt, and molten metallic iron within a growing Earth would produce a proto-atmosphere enriched in H_2 and CH_4 when most accreting materials are reduced like enstatite meteorites. Referring to their results, we assume that the Earth's proto-atmosphere consists of H_2 and CH_4. The CH_4/H_2 ratio is taken to be a parameter because of the uncertainty in their supply to the proto-Earth and possible change through time due to selective loss and supply.

4.2 Results

4.2.1 Atmospheric profiles

Figures 4.1 show the radial profiles of mean velocity, temperature, number density, radiative heating rate, radiative cooling rate and reaction rate for typical steady state solutions. In each solution, the flow is radially accelerated from near zero velocity to supersonic (figure 4.1(a)). Here we focus on the profiles of CH_4 and its photochemical products which are important for the atmospheric energy balance by their radiative cooling in the lower region ($r < 1.3R_{\rm Earth}$). CH_4 is rapidly dissociated into CH and CH_3 when $CH_4/H_2 = 0.001$ (figure 4.1(c)). This behavior is unchanged for higher CH_4/H_2 cases. As shown in Figure 4.1(f) which represents the rates of reactions that break down CH_4, the main paths of CH_4 broken down are the following reactions:

$$CH_4 + h\nu \rightarrow CH_2 + H_2, \tag{4.1}$$

$$CH_4 + h\nu \rightarrow CH_2 + H + H, \tag{4.2}$$

$$CH_4 + H^+ \rightarrow CH_4^+ + H, \tag{4.3}$$

$$CH_4 + H^+ \rightarrow CH_3^+ + H_2. \tag{4.4}$$

CH_4 is broken down by the reactions with ions as well as by photolysis, as known for the ionospheres of Jupiter and Saturn (e.g. Yung and Demore, 1998). Our Earth atmosphere model shows higher efficiency of CH_4 decomposition than the Mars atmosphere model (Chapter 3) because the effect of photolysis becomes large under the slower advection on Earth with the deeper gravitational well. H^+ , the major reactant for CH_4 decomposition, is produced by photoionization of H_2:

$$H_2 + h\nu \rightarrow H^+ + H + e. \tag{4.5}$$

Thus, the mixing fraction of CH_4 is anticorrelate with that of H^+ as shown in figure 4.1(c) and 4.1(d). On the other hand, the decreasing trend in CH_4 becomes modest in

$r > 1.3R_{\rm Earth}$ because the temperature increase enhances the formation reaction of CH_4 described by

$$H_2 + CH_3 \rightarrow CH_4 + H. \tag{4.6}$$

4.2.2 Energy balance

Figure 4.2 represents the energy balance in the subsonic region. The heating efficiency is given by equation (3.3). $\sim 75\,\%$ of the energy obtained by the XUV absorption is lost by the chemical expense and the radiative cooling by H_3^+ almost independently of CH_4 mixing ratio. The radiative cooling by CH and CH_3 produced by photolysis of CH_4 has a great effect on the atmospheric energy balance. In the region near the lower boundary, the radiative cooling by CH_3 occurs efficiently because CH_3 is infrared active even at low temperature (figure 3.5). At altitudes with increased temperature, the effect of radiative cooling by CH also becomes effective (figure 3.5). The heating efficiency decreases as the basal CH_4/H_2 ratio increases: the heating efficiency drops to ~ 0.05 when $CH_4/H_2 = 0.007$ (figure 4.2). The change in the heating efficiency shows radiative cooling by CH and CH_3 suppresses atmospheric escape significantly even when basal CH_4 mixing ratio is small.

4.2.3 Escape rate and mass fractionation

Figure 4.3 represents the dependence of the escape mass fluxes of main gas species on the basal CH_4/H_2 ratio. Here, the bulk escape molecular fluxes F_i and mass fluxes $F_{m,i}\,(i = H_2, CH_4)$ are related as follows

$$F_{m,i} = m_i F_i = m_i 4\pi r_0^2 n_i(r_0) v_i(r_0), \tag{4.7}$$

where m_i and v_i are the molecular mass and velocity of species i. Note that the dissociation of these species are negligible at the lowest boundary $r = r_0$. As the basal CH_4/H_2 ratio increases, the escape mass flux decreases because the heating efficiency decreases by radiative cooling. The dashed line in figure 4.3 represents the critical flux representing

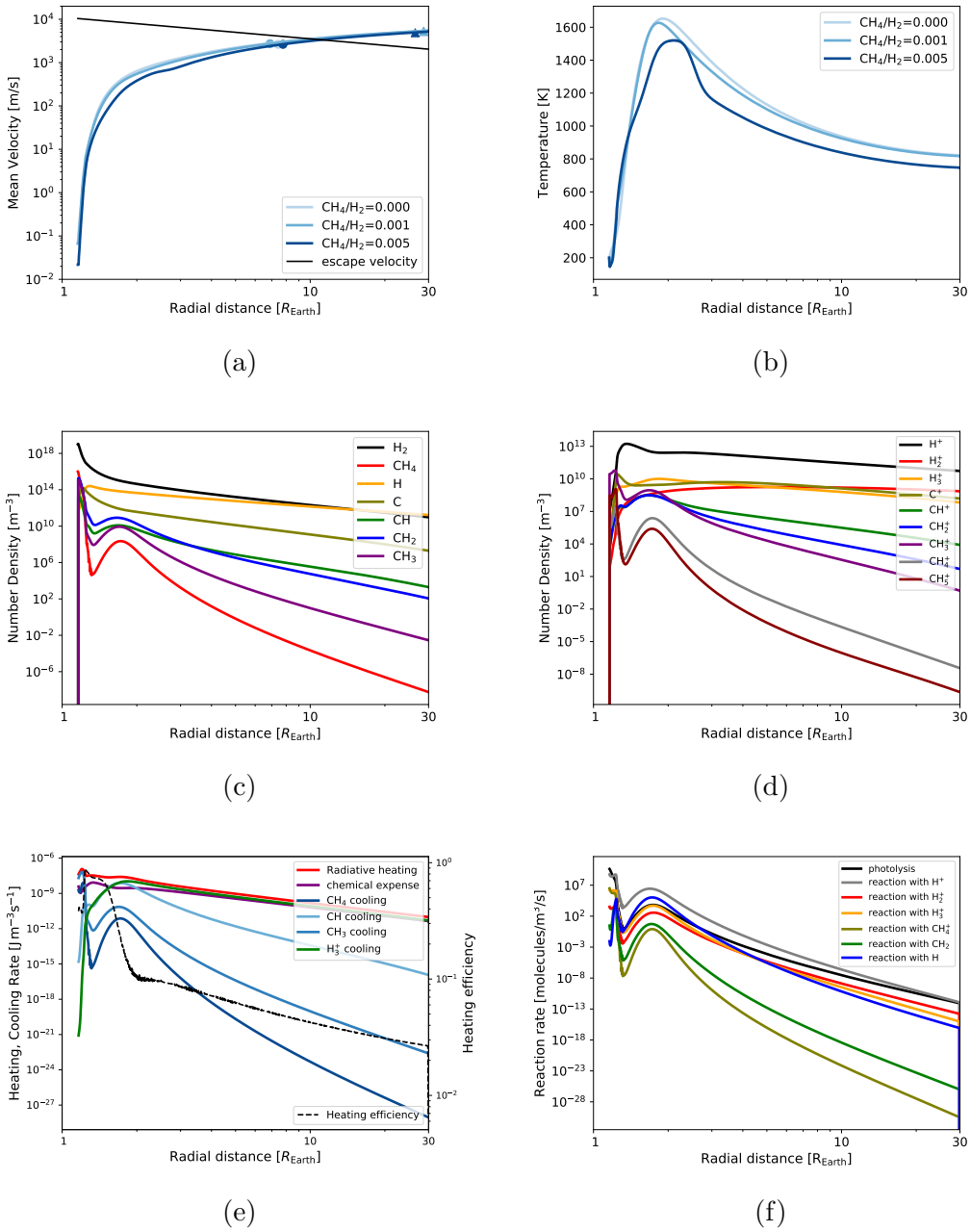

Figure 4.1: Atmospheric profiles. (a) Mean velocity. The dots represent the transonic points. The black line represents the escape velocity. (b) Temperature. (c) Number density of neutral species. (d) Number density of ion species. (e) Radiative heating and radiative cooling rate. (f) Reaction rates of reactions which break down CH_4. The results in (c)–(f) are obtained when $CH_4/H_2 = 0.001$.

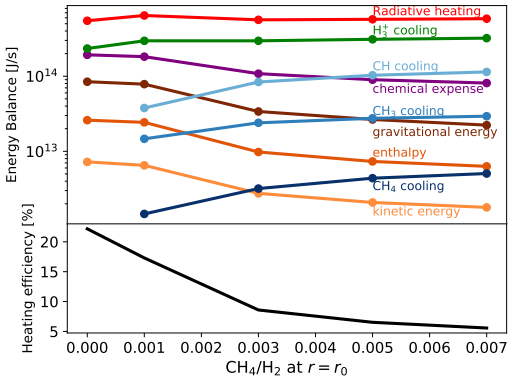

Figure 4.2: Energy balance in the subsonic region. "kinetic energy" is the flux of kinetic energy, "enthalpy" is the flux of enthalpy, "gravitational energy" is the difference of the gravitational potential, "Radiative heating" is the heating rate by XUV absorption, "chemical expense" is the net chemical expense of energy, and "CH_4 cooling", "CH cooling", "CH_3 cooling" and "H_3^+ cooling" are the radiative cooling rate by CH_4, CH, CH_3 and H_3^+ respectively. The black line in the lower panel represents the heating efficiency.

the minimum flux of H_2 that can drag CH_4 to space. The critical flux, $F_{\rm crit}$, is derived from the crossover mass which is the largest molecular mass of secondary species that can be dragged upward by the dominant lighter gas. Taking $m_c = m_{\rm CH_4}$,

$$F_{\rm crit} = \frac{b_{\rm H_2,CH_4} g X_{\rm H_2}}{kT}(m_{\rm CH_4} - m_{\rm H_2}). \tag{4.8}$$

When extrapolating the H_2 escape rate linearly using the values when CH_4/H_2=0.005 and 0.007, the H_2 flux reaches the critical flux when the CH_4/H_2 ratio increases to 0.012. This means that only H_2 escapes to space leaving CH_4 behind when $CH_4/H_2 \gtrsim 0.012$ under the assumed XUV flux.

The fractionation factor given by $(F_{\rm CH_4}/F_{\rm H_2})/(n_{\rm CH_4}(r_0)/n_{\rm H_2}(r_0)) = v_{\rm CH_4}(r_0)/v_{\rm H_2}(r_0)$ depends on the basal CH_4/H_2 ratio as shown in figure 4.4. As the basal CH_4/H_2 ratio increases, the fractionation factor decreases, i.e., the mass fractionation between H_2 and CH_4 occurs more remarkably. The dashed line of figure 4.4 is obtained from equation (3.8), which approximates the numerical results represented by the solid line.

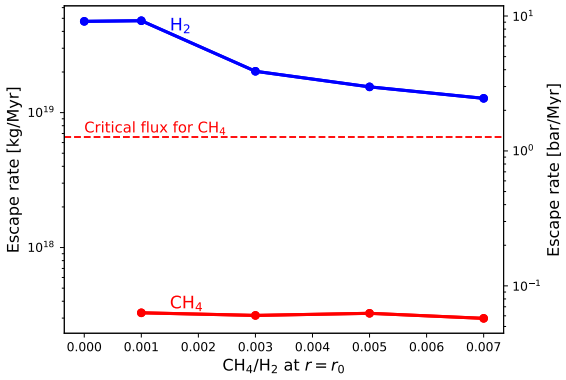

Figure 4.3: Escape mass fluxes of main gas species per 1 Myr as a function of the basal CH_4/H_2 ratio. The right vertical axis represents the flux normalized by the mass of the present Earth's atmosphere: $1\,\mathrm{bar} = 5.3 \times 10^{18}\,\mathrm{kg}$. The blue line represents the H_2 mass flux, and the red line represents the CH_4 mass flux. The dashed line represents the critical flux which is the minimum flux of H_2 that can drag CH_4 upward.

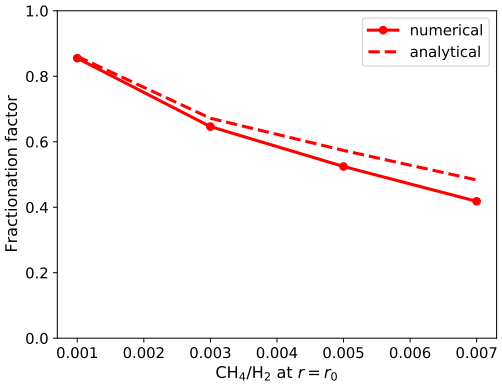

Figure 4.4: Fractionation factor given by $v_{\mathrm{CH_4}}(r_0)/v_{\mathrm{H_2}}(r_0)$ as a function of the basal CH_4/H_2 ratio. The solid line represents the value from the numerical results, and the dashed line represents the value from the crossover mass.

4.2.4 Dependence of heating efficiency and atmospheric escape rate on XUV flux

In the previous section, we apply the XUV spectrum whose total flux is about 100 times the present. However, there remains significant uncertainty in the XUV flux of the early Sun (Tu et al., 2015). Here, we show the results when the XUV flux is twice or three times as large as that of the standard-setting. Figure 4.5 represents the atmospheric escape rates and heating efficiencies normalized by the standard values. The atmospheric escape rate does not increase proportionally with the XUV flux simply, but the increasing trend in the escape rate weakens as the XUV flux and the CH_4/H_2 ratio increase. This is because heating efficiency decreases due to the increase in the photolysis production of CH and CH_3.

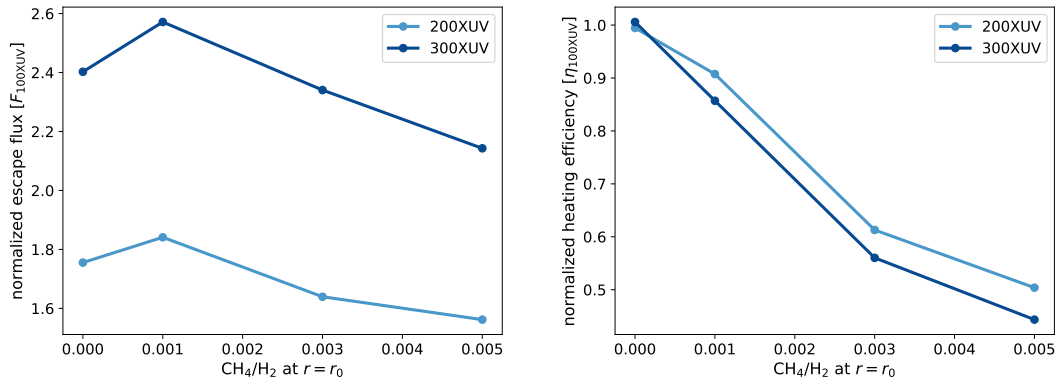

(a) (b)

Figure 4.5: (a) Escape fluxes normalized by the standard value. (b) Heating efficiencies in the subsonic regions normalized by the standard value.

4.3 Discussion

4.3.1 Evolution of early atmosphere on Earth

Initial conditions and possible evolutionary tracks of escaping atmosphere

Significant decrease in heating efficiency suggested from our numerical results implies a prolonged Earth's proto-atmosphere with reduced composition. The evolution of a proto-atmosphere on Earth by hydrodynamic escape may be constrained by the current inventories and the isotopic compositions of volatiles on the Earth's surface. Here we will argue possible evolutionary tracks of proto-atmosphere starting from a H_2 and CH_4-rich atmosphere.

To make an analysis applying our simulations of hydrodynamic escape, it is assumed that all carbon in the lower atmosphere is in the form of CH_4 and the middle atmosphere is dominated by H_2 and CH_4 with the possible existence of H_2O in the lower atmosphere and the proto-ocean on the surface. As the standard-setting, constant XUV flux about 100 times the present is given and the processes of atmospheric supply and non-hydrodynamic escape during the evolution of the proto-atmosphere are neglected.

We use the escape flux and the fractionation factor in figure 4.4 to describe the change in the atmospheric amount. The fractionation factor in figure 4.4 is approximated by the following fitting function:

$$\frac{F_{\mathrm{CH_4}}/F_{\mathrm{H_2}}}{n_{\mathrm{CH_4}}(r_0)/n_{\mathrm{H_2}}(r_0)} = \frac{1}{1+af}, \tag{4.9}$$

where a is the fitting factor and $f = n_{\mathrm{CH_4}}(r_0)/n_{\mathrm{H_2}}(r_0)$. The fractionation factor of CH_4 of figure 4.4 can be fitted by $a = 1.85 \times 10^2$. Using the same method described in chapter 3, the change in the amount of atmospheric H_2 and CH_4 can be calculated.

An estimated amount of carbon on the present Earth's surface is equivalent to ∼70 bar of CO_2 (Holland, 1978). Here, we assume that CH_4 with the total amount of carbon equivalent to 70 bar of CO_2 was left behind when the hydrodynamic escape of CH_4 stopped. We stop the escape of CH_4 when the CH_4/H_2 ratio increases to 0.012 at which the H_2 flux decreases to the critical flux for CH_4 loss.

Nitrogen species are likely lost by hydrodynamic escape as well as carbon species. It is unknown what is the main nitrogen species in the proto-atmosphere, thus we consider two cases: when N_2 is the main species and when NH_3 is the main species in the proto-atmosphere. We assume that nitrogen species with the total amount of nitrogen equivalent to 0.8 bar of N_2 was left behind when escape of nitrogen species stopped. In this study, the nitrogen species are treated as trace species which have negligible effects on the hydrodynamic escape. The change in atmospheric amounts of nitrogen species is calculated by equation (3.16).

Under the CH_4 enriched conditions where no CH_4 escapes, the H_2 escape flux is given by the critical flux for CH_4 described by equation (4.8) since the cease of uplift of CH_4 would prevent the heating efficiency from dropping further. This assumption is applied when the CH_4/H_2 ratio > 0.012.

Isotopic fractionation of carbon, nitrogen and hydrogen can be also calculated. The $^{13}C/^{12}C$ ratio, $^{15}N/^{14}N$ ratio, and D/H ratio are given by

$$\frac{^{13}\mathrm{C}}{^{12}\mathrm{C}} = \frac{N_{^{13}\mathrm{CH_4}}}{N_{\mathrm{CH_4}}} \tag{4.10}$$

$$\frac{^{15}\mathrm{N}}{^{14}\mathrm{N}} = \begin{cases} \frac{N_{^{15}\mathrm{NH_3}}}{N_{^{14}\mathrm{NH_3}}} \\ \frac{N_{^{15}\mathrm{N}^{14}\mathrm{N}}}{2N_{^{14}\mathrm{N_2}}+N_{^{15}\mathrm{N}^{14}\mathrm{N}}} \simeq \frac{N_{^{15}\mathrm{N}^{14}\mathrm{N}}}{2N_{^{14}\mathrm{N_2}}} \end{cases} \tag{4.11}$$

$$\left(\frac{\mathrm{D}}{\mathrm{H}}\right)_{\mathrm{atomsphere}} = \frac{N_{\mathrm{HD}}}{2N_{\mathrm{H_2}} + N_{\mathrm{HD}}} \simeq \frac{N_{\mathrm{HD}}}{2N_{\mathrm{H_2}}} \tag{4.12}$$

$$\left(\frac{\mathrm{D}}{\mathrm{H}}\right)_{\mathrm{ocean}} = \frac{N_{\mathrm{HDO}}}{2N_{\mathrm{H_2O}} + N_{\mathrm{HDO}}} \simeq \frac{N_{\mathrm{HDO}}}{2N_{\mathrm{H_2O}}} \tag{4.13}$$

Using equations (4.10), (4.11), (4.12), (4.13) and the atmospheric evolutionary tracks of H_2 and CH_4, changes in isotopic ratios can be calculated.

As for the evolution of the D/H ratio, we take into account liquid H_2O mass stored in ocean, which would have effects to buffer the D/H fractionation in the proto-atmosphere. The following deuterium exchange reaction is assumed to be in equilibrium among atmospheric H_2 and oceanic water referring to Genda and Ikoma (2008):

$$\mathrm{HD} + \mathrm{H_2O} \leftrightarrow \mathrm{HDO} + \mathrm{H_2}. \tag{4.14}$$

The equilibrium constant for this reaction is given by

$$K \simeq \frac{(\mathrm{D/H})_{\mathrm{ocean}}}{(\mathrm{D/H})_{\mathrm{atmosphere}}} = \frac{0.22 \times 10^6}{T^2} + 1 \tag{4.15}$$

where T is the temperature (Richet et al., 1977; Genda and Ikoma, 2008). The seawater mass is taken to be constant at the present value. The surface temperature refers to the results of Pahlevan et al. (2019) to determine the surface temperature T: they indicated that greenhouse warming by inventories of $\sim$ 1–100 bars of equivalent H_2 yields surface temperatures $\sim$ 300–550 K by applying their climate model on H_2-H_2O atmospheres.

The initial isotopic compositions of carbon and nitrogen of the proto-atmosphere are taken in the range of the values of primitive meteorites supposing that primitive meteorites are analog of building blocks providing volatiles to Earth. The isotopic compositions of carbon and nitrogen on the present Earth are known to be close to those of primitive meteorites: the $^{13}C/^{12}C$ ratios of primitive meteorites are within the factor from 0.98 to 1.01 of the representative value of the Earth's mantle (Des Marais, 2001; Kerridge, 1985; Marty et al., 2013) and the $^{15}N/^{14}N$ ratios of primitive meteorites are within one from 0.95 to 1.335 of the value of the present Earth's atmosphere (Kerridge, 1985; Grady and Wright, 2003; Furi and Marty, 2015). The D/H ratio of the seawater is also close to those of carbonaceous chondrites (e.g. Marty, 2012). The initial D/H ratio of the seawater is highly uncertain among the values of the solar nebula gas, primitive meteorites, and comets. As for the D/H ratio, therefore, its enhancement relative to the initial ratio by hydrodynamic escape is analyzed.

Figure 4.6 shows an evolutionary track of proto-atmosphere that satisfies the present amounts and isotopic compositions of carbon and nitrogen on Earth. For convenience, the atmospheric mass of each species is expressed by the equivalent surface pressure given by

$$P_i = \frac{M_i g}{4\pi R_p^2}, \tag{4.16}$$

where P_i and M_i are the equivalent surface pressure and atmospheric mass of species i, and g and R_p are the surface gravity and radius of Earth. The result shown in figure 4.6

is obtained for the case when the initial amount of H_2 is taken maximum. More initial H_2 causes excessive isotopic fractionation of carbon and nitrogen.

The dependence of initial atmospheric amounts on initial CH_4/H_2 ratio is shown in Figure 4.7. Here, the initial H_2 amount is estimated so as the hydrodynamic escape to leave behind carbon and nitrogen with the present inventories. Figure 4.8 represents the relationship between initial isotopic composition and final isotopic composition. CH_4 and nitrogen species hardly escape compared to H_2 (figure 4.6, 4.7) because their escape must be suppressed to satisfy the constraint of the initial isotopic compositions of carbon and nitrogen (figure 4.6, 4.8). On the other hand, the upper limit of H_2 loss is equivalent to ~ 400 bar, indicating that a massive hydrogen-rich proto-atmosphere was possibly formed (figures 4.6, 4.7). This owes to the suppression of escape of CH_4 and nitrogen species by the effect of radiative cooling.

The formation of a massive hydrogen-rich atmosphere on proto-Earth has been suggested from the chemistry of the building blocks of Earth. As described in the previous section, most of Earth's building blocks were closest to enstatite meteorites, possessing the most reduced oxidation state among primitive meteorites (Dauphas, 2017). In such a case, the H_2/H_2O ratio of impact-generated vapor becomes ≥ 10 considering the reduction of water to hydrogen by Fe metal (Kuramoto and Matsui, 1996). The amount of hydrogen accreted on Earth is highly uncertain. To explore its possible range, we first apply the two-component model (Dreibus and Wanke, 1987) that assumes the building block to be a mixture of a highly reduced volatile-free component A and an oxidized volatile-rich component B. Assuming that A:B=9:1 referring to Dreibus and Wanke (1987) and the component B contains 10 wt% H_2O referring to the compositions of CI chondrites (e.g. Marty, 2012), the amount of H is $1.1 \times 10^{-3}\, M_{\rm Earth}$ (equivalent to 1.3×10^3 bar).

The oceanic D/H ratio increases larger than the atmospheric D/H ratio because of deuterium enrichment via deuterium exchange reaction (figure 4.6, 4.8). If the main sources of terrestrial water are materials like carbonaceous chondrites, the initial D/H ratio of the entire system should be close to the value of carbonaceous chondrites. In such a case, the significant elevation of oceanic D/H ratio caused by hydrogen escape

seems inconsistent with the present value (Pahlevan et al., 2019). However, this result strongly depends on assumptions. We assume that the amount of the seawater is constant at the present value, but it may have been larger and or experienced exchange with large water reservoirs in the interior on early Earth. In this case, the elevation of the oceanic D/H ratio would be significantly suppressed. The oceanic D/H ratio also depends on the assumed surface temperature. Here we apply the surface temperature obtained from the climate model composed of H_2 and H_2O. However, the greenhouse effect may significantly increase considering the effect of other greenhouse gases such as CH_4 and NH_3, which also affects to dilute the concentration of deuterium in the ocean. The D/H ratio may be diluted by the supply of hydrogen by late accretion. Moreover, the assumption that the initial D/H ratio is close to the value of carbonaceous chondrites should be reconsidered. If proto-planets obtained hybrid-type atmospheres composed of the solar component and the degassed component, the D/H ratio may become smaller than the value of carbonaceous chondrites due to the effect of the solar component. Thus, it is possible to settle into the present ocean D/H ratio even if the massive hydrogen-rich atmosphere was formed.

Earth may have obtained solar nebula gas as well as impact-generated vapor (Ikoma and Genda, 2006). But, the amount of acquired nebula gas seems limited because the concentration of noble gases in the solar nebula is much larger than that in the present Earth's atmosphere and noble gases cannot escape by hydrodynamic escape as our study indicates. In order to explain the amount of Ne in the present Earth's atmosphere, the amount of obtained nebula gas needs to be lower than ~ 0.1 bar assuming no Ne escape.

The timescale for H_2 escape depends on the initial CH_4 ratio and initial amounts of H_2 as shown in figure 4.9. The maximum timescale for H_2 escape is ~ 400 Myr (figure 4.6, 4.9), which is about one order of magnitude longer than that for almost pure hydrogen atmosphere. The actual timescale may become longer than the above results because the H_2 escape flux after CH_4 escape stops is taken to the critical flux, which is the upper limit. Our result implies that a hydrogen-rich environment had been kept during Hadean and possibly until early Archean, which may have an important role in warming early

Earth and the origin of life as described in detail later.

Effect of uncertainties in assumptions on estimated atmospheric evolution

XUV flux As mentioned previously, there remains significant uncertainty in the XUV flux of the early Sun. Since the escape flux depends on the XUV flux, we assess the atmospheric evolution under different XUV flux. Figure 4.10 represents the timescale for H_2 escape using results given XUV flux twice as large as the standard-setting. The maximum initial amount of H_2 to satisfy the constraints of isotopic compositions decreases as the XUV flux increases because escape and isotopic fractionation of carbon and nitrogen species can occur more easily. As a result, the maximum timescale for H_2 escape shortens slightly: the maximum timescale for H_2 escape is $\sim$ 250 Myr under the doubled XUV flux, which is about 0.7 times that the result under the standard XUV flux.

Atmospheric escape before Earth reached the present mass So far we have assumed implicitly that no atmospheric escape occurred before the end of planetary accretion. However, proto-planets that presumably conglomerated to Earth might have experienced atmospheric escape (Odert et al., 2018). The results in chapter 3 suggest that the isotopic fractionation of H and C may have proceeded in proto-atmospheres on Mars-sized proto-planets and the degree of fractionation highly depends on the initial atmospheric mass and composition. The duration of escape, i.e., the period exposed to the solar XUV for such a proto-planet is another important factor. If it was short, atmospheric loss little proceeds as well as isotopic fractionation.

Supply and other removal processes of volatiles The late accretion may play an important role in the supply of volatiles. After the moon-forming giant impact event, Earth may have continued to accrete materials, amounting to about 0.5% of its present mass (Walker et al., 2015). The composition of accreted materials is uncertain. From the analysis of Ru isotope compositions of the mantle and meteorites, Fischer-Godde and Kleine (2017) estimated that these materials were like enstatite chondrites. On the other

hand, from the same analysis extended to Eoarchaean ultramafic rocks, the same group estimated that these materials were like carbonaceous chondrites (Fischer-Godde et al. 2020). If most accreted materials are like carbonaceous chondrites with 10 wt% H_2O and carbon and nitrogen in proportion C/H=1/5 and N/C=1/30, the late accreted H, C and N reach $\sim 3 \times 10^{20}$ kg, $\sim 4 \times 10^{20}$ kg and $\sim 1 \times 10^{19}$ kg respectively. The supply of volatiles by the late accretion may dilute the isotopic fractionation, which relaxes the constraint of isotopic composition and increases the upper limit of the amount of initial atmosphere and the timescale for H_2 escape. For example, when we assume that carbon equivalent to 30 bar of CO_2 was provided by the late accretion, the upper limit of the initial amount of H_2 and that of the timescale for H_2 escape become ~ 1.4 times larger.

Duration of reduced environment may have been prolonged by generation of reduced gas by late accretion. In particular, massive H_2 may have formed if materials like enstatite chondrites were accreted and H_2O on Earth was reduced. Assuming that 30 wt% metallic iron is included in accreted materials and all metallic iron reacts with H_2O, $\sim 2 \times 10^{20}$ kg equivalent to ~ 40 bar of H_2 is formed and the duration of H_2 is prolonged for ~ 50 Myr at least, which is calculated by the critical flux when $X_{H_2} = 1$ described by equation (4.8).

In contrast, meteoroid bombardment may have induced atmospheric escape by impact erosion (Vickery and Melosh,1990). The degree of the impact erosion of Earth's atmosphere throughout its history is difficult to estimate accurately. However, the effect of impact erosion on Earth reaching the present mass seems limited because the large mass of Earth and the massive atmosphere at the early stage decrease its efficiency (Vickery and Melosh,1990).

The cycle of volatiles between the surface and the interior also may have affected the amounts and compositions of volatiles on the surface. The mantle may contain a significant amount of carbon and nitrogen as well as water: the amounts of water, carbon, and nitrogen in the mantle are estimated to be $1 - 10$ times larger than the ocean mass (e.g. Genda, 2016), several times to several ten times larger than that on the surface (e.g. Hirschmann, 2018), and several times larger than that in the atmosphere (e.g. Johnson

and Goldblatt, 2015) respectively. If the cycle of volatiles between the surface and the interior has occurred efficiently, the isotopic fractionation of volatiles on the surface and atmosphere may have been diluted. Considering the cycle of volatiles also increases the estimated atmospheric evolutionary track as well as the late accretion.

We assumed that the lower atmosphere always consisted of H_2 and CH_4. But, the composition in the lower atmosphere may have changed by photochemistry. Zahnle et al. (2020) estimated the photochemical evolution of impact-generated H_2-CH_4 atmospheres by a zero-dimensional photochemical model. CH_4 is converted into CO, CO_2, and organic matters within several ten million years when the atmosphere composed of 35 bar of H_2 and 14 bar of CH_4 is formed. Nitrogen species are also converted into nitriles, and amines. In this case, the atmospheric amount and isotopic composition change by accumulation of produced CO_2 and organic matters on the surface, which affects the estimated atmospheric evolutionary track. However, the photochemistry in the lower atmosphere enriched in H_2 needs to be more investigated because formation reactions of CH_4 and NH_3 by H may become effective and make them stable photochemically as in the mesosphere region of the giant planets (Yung and DeMore, 1998).

As described above, there are a lot of processes that affect atmospheric evolution. Therefore, it is difficult to constrain the atmospheric evolution from the amount of volatiles and isotopic compositions accurately. But the conclusion that the maximum timescale for H_2 escape is longer than several hundreds Myr does not change even when more strict constraints that carbon species and nitrogen species must not escape is used considering that the isotopic compositions of carbon and nitrogen on Earth are close to those of primitive meteorites.

Effects of prolonged reduced environment on early Earth

Our results indicate that a hydrogen-rich reduced environment had been kept during Hadean and possibly until early Archean. The reduced species such as H_2 and CH_4 may have contributed to warming early Earth: hydrogen can also contribute to warm Earth by collision-induced absorption (Sagan and Mullen, 1972; Ramirez et al., 2014). The geologic

record indicates that liquid water was present on early Earth (e.g., Mojzsis et al.,2001) even though the Sun was $\sim 30\%$ less luminous on the early stage (e.g., Gough,1981). The long-lasting reduced environment can explain the warm climate with the liquid ocean on early Earth.

The early hydrogen-rich reduced atmosphere may have played an important role in producing organic matters linked to the emergence of living organisms because the hydrogen-rich environment where organic matters were produced efficiently may have lasted until ~ 4 billion years ago when life is expected to have emerged (Rosing, 1999). Schlesinger and Miller (1983) indicated that HCN and H_2CO, which are precursors to amino acids, sugars, and nucleobases, are produced efficiently when $H_2/C > 1$. Once HCN and H_2CO dissolved in the ocean, amino acids, sugars, and nucleobases could have been formed (Schlesinger and Miller, 1983). Besides, high-molecular organic matters were likely formed in the reduced atmosphere containing CH_4 and nitrogen species by photochemistry. Hydrocarbons, nitriles, and organic haze aerosols are synthesized through photolysis of CH_4 and N_2 in the Titan's atmosphere (Wilson and Atreya, 2003). These organic matters formed in the atmosphere would have been deposited in the ocean. As a result, an organic soup in the ocean may have been formed, and eventually it may have led to the emergence of living organisms.

4.3.2 Comparison of the hydrodynamic escape of reduced proto-atmospheres on Earth with that on Mars

We have applied our hydrodynamic escape model to both reduced proto-atmospheres on Earth and those on Mars. The effect of radiative cooling by infrared active species on Earth's atmospheres is more drastic than that on Mars: in the case of the Earth's atmospheres, radiative cooling by photochemical products such as H_3^+, CH and CH_3 suppresses atmospheric escape significantly even though their concentrations are small (figure 3.4). The difference between hydrodynamic escape on Earth and that on Mars is mainly due to the difference of the planetary mass and the gravity. The gravity is small

relatively and adiabatic cooling is easy to become effective on Mars, leading to the lower atmospheric temperature and inefficient radiative cooling.

The amount of atmospheric species heavier than H_2 on Mars becomes more than one order of magnitude smaller via hydrodynamic escape when the mixing ratio of H_2 was larger than $\sim 90\,\%$ (figure 3.17). On the other hand, atmospheric species heavier than H_2 on Earth escape hardly even when the mixing ratio of H_2 is $\sim 99\,\%$. The difference in the efficiency of hydrodynamic escape may have resulted in a significant difference in the amount of volatiles on their surfaces.

4.4 Conclusion

We have applied our one-dimensional hydrodynamic escape model to Earth's proto-atmosphere consisted of H_2 and CH_4. CH_4 is dissociated rapidly by photolysis and reactions with ions. The atmospheric escape rate decreases significantly as the mixing ratio of CH_4 increases mainly because of the energy loss by radiative cooling by H_3^+, CH and CH_3 produced photochemically. Heavier species other than H_2 cease to escape and only H_2 escapes when $CH_4/H_2 \gtrsim 0.01$. The maximum timescale for H_2 escape to satisfy the constraints of the isotopic compositions and the amount of volatiles on the present Earth becomes more than ~ 100 Myr. Our results suggest that a hydrogen-rich reduced environment had been kept and played an important role in producing a warm climate and organic matters linked to the emergence of living organisms on early Earth.

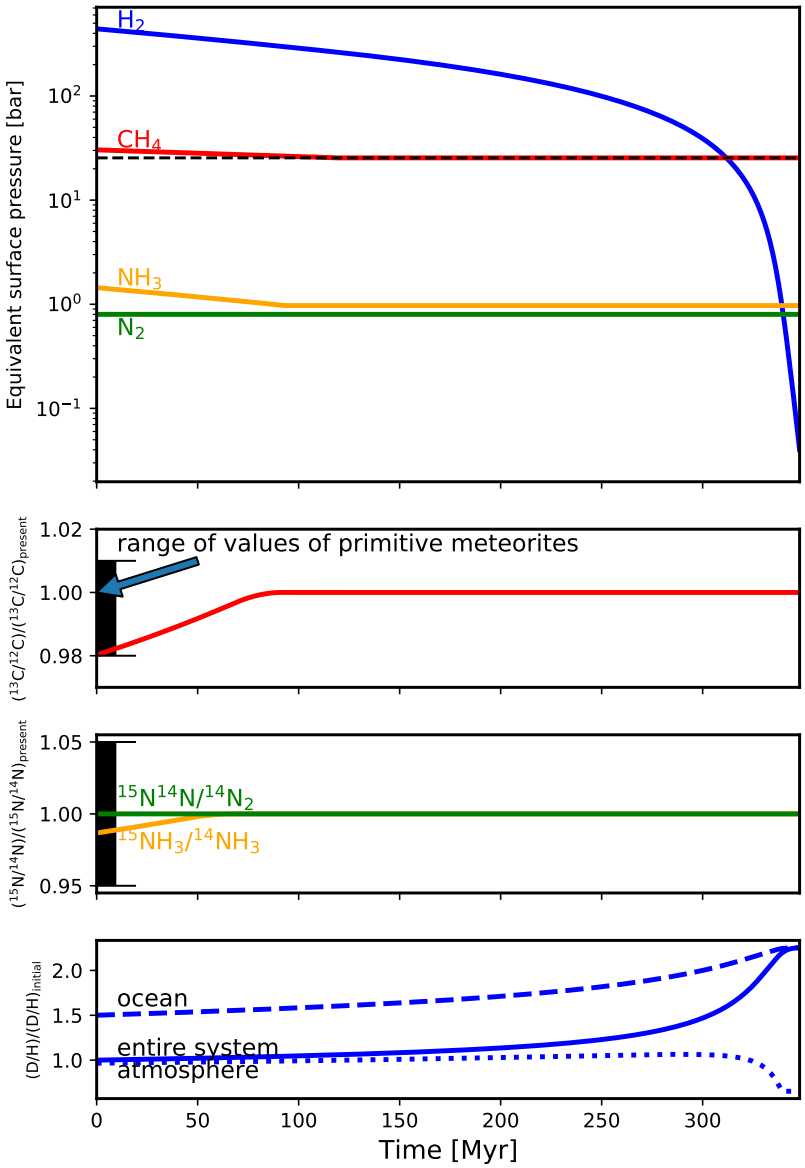

Figure 4.6: Possible changes in the amount and the isotopic compositions of the atmosphere over time when the atmospheric loss and the timescale for H_2 escape are maximum.

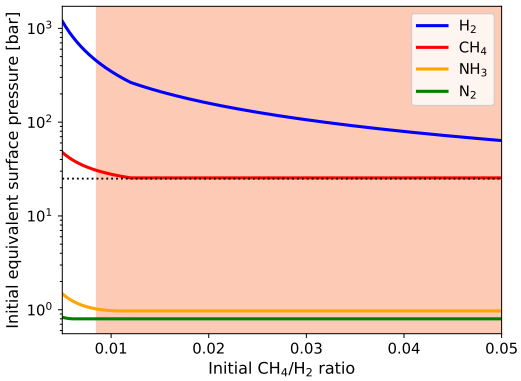

Figure 4.7: Initial atmospheric amounts with initial CH_4/H_2 ratio. The blue line, red line, orange line and green line represent the amounts of H_2, CH_4, NH_3 and N_2 respectively. The shaded area represents the range to satisfy the constraints of isotopic compositions.

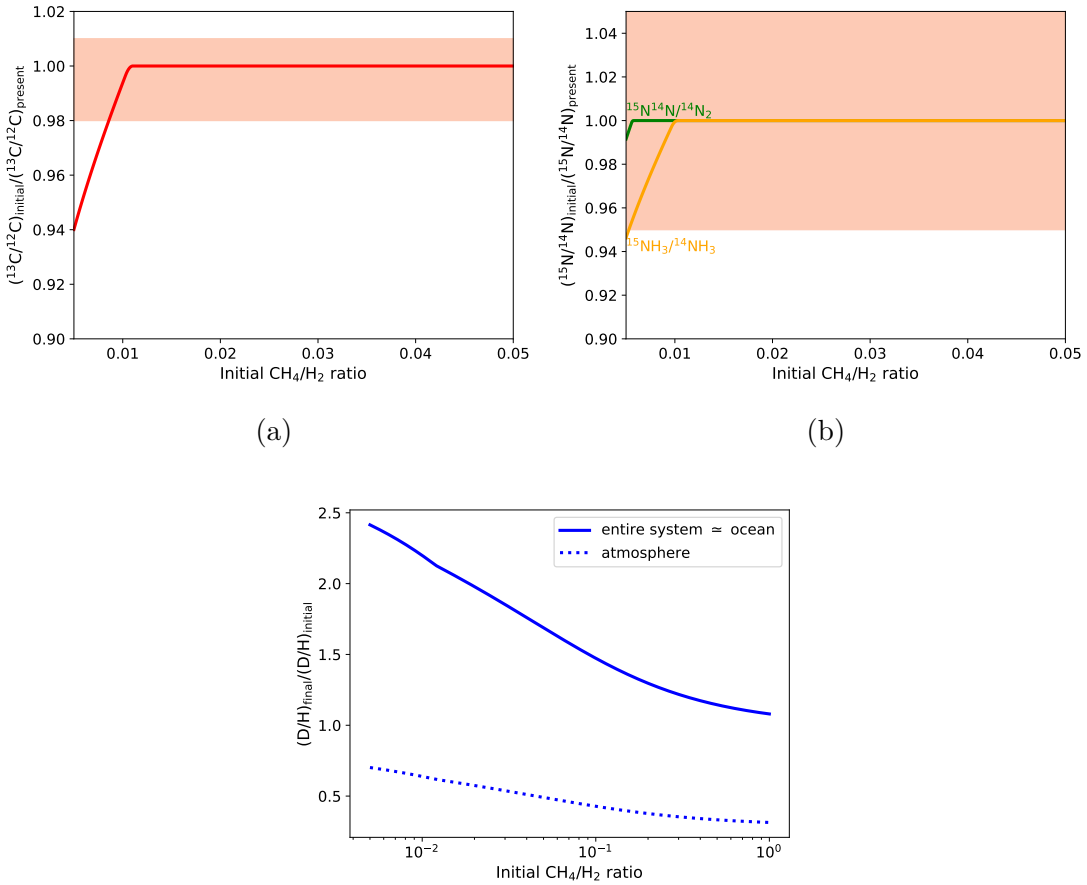

(a) (b)

(c)

Figure 4.8: (a) Ratio of initial $^{13}C/^{12}C$ ratio to the present $^{13}C/^{12}C$ ratio. (b) Ratio of initial $^{15}N/^{14}N$ ratio to the present $^{15}N/^{14}N$ ratio. $^{15}N/^{14}N = N_{^{15}N^{14}N}/(2N_{^{14}N_2} + N_{^{15}N^{14}N})$ and $^{15}N/^{14}N = N_{^{15}NH_3}/N_{^{14}NH_3}$ are assumed on the green line and on the orange line respectively. (c) Ratio of final D/H ratio to initial D/H ratio. The shaded area on (a) and (b) represents the range of the values of primitive meteorites.

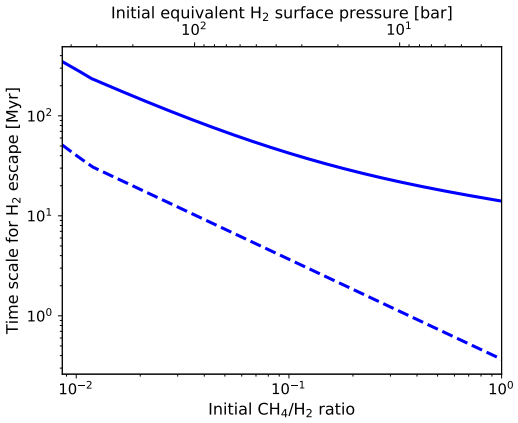

Figure 4.9: Timescale for H_2 escape as a function of initial CH_4/H_2 ratio and initial amounts of H_2. The solid line represents the timescale for H_2 escape estimated from the atmospheric evolutionary tracks. The dashed line represents the timescale for H_2 escape calculated by dividing the initial H_2 amount by the escape rate of pure hydrogen atmosphere.

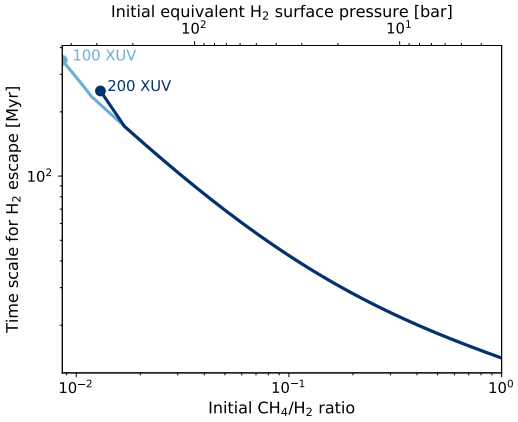

Figure 4.10: Timescale for H_2 depending on the XUV flux.

Chapter 5

Conclusion

The evolution of H_2-rich proto-atmospheres on Mars and Earth is theoretically explored by applying a newly developed one-dimensional hydrodynamic escape model that includes radiative processes and photochemical processes for a multi-component atmosphere. Judging from recent planet formation theory, chronometry of martian meteorites and geochemical constraints on the type of planetary building blocks, the formation of proto-atmospheres enriched in H_2-CH_4 on Mars and Earth is very likely. Such H_2-rich atmospheres suffer hydrodynamic escape caused by enhanced solar XUV radiation and therefore should eventually lose reduced gas species and be replaced by an atmosphere with oxidized compositions. Duration of reduced proto-atmosphere is an important issue to understand the early surface environments on both planets because reduced gas species possibly act as the effective source of organic macromolecules precursory of life and greenhouse gases that allow surface liquid water under the faint young Sun. Previous modeling studies favored the loss of H_2 in a short time scale $\sim$ 10 Myr, but large uncertainty remained in this estimation because the possible slowdown of escape caused by radiative cooling of infrared active species was neglected.

Our new numerical model precisely incorporating the radiative and photochemical processes shows that the radiative cooling by infrared active species has profound effects to suppress the escape rate from the H_2-rich atmosphere. In escaping outflow on Mars, a significant fraction of molecules is found to stay undissociated even under the intense

solar XUV environment. As the mixing ratio of CH_4 and CO increases above ~ 0.1, the escape rate of reduced Martian atmospheres decreases more than one order of magnitude compared to the pure H_2 atmosphere, and the mass fractionation occurs more remarkably primarily because of the radiative cooling by survived CH_4 and CO. The total amount of carbon species lost by hydrodynamic escape exceeds 10 bar equivalent to 20 bar of CO_2 when the proto-Mars obtained $\gtrsim 10$ bar of H_2 assuming that carbon species equivalent to 1 bar of CO_2 was left behind when most H_2 completed its hydrodynamic escape. The timescale for H_2 escape from H_2-CH_4-CO atmospheres becomes about one order of magnitude longer than that from pure hydrogen atmospheres especially when the CH_4/CO ratio is high. If the proto-Mars obtained > 100 bar of H_2, the timescale for H_2 escape exceeds ~ 100 Myr, which implies that a reduced environment allowing surface deposition of organic matters produced by atmospheric chemistry may have been kept on early Mars at eras traceable from geologic records. Our results also suggest that atmospheres on Mars-sized proto-planets survived during the giant impact phase and would merge into the atmospheres of the terrestrial planets experienced proto-planet collisions.

In contrast to the results of Mars, CH_4 is dissociated rapidly by photolysis and reactions with ions in escaping outflow on Earth due to the deeper gravitational well. The atmospheric escape rate decreases significantly as the mixing ratio of CH_4 increases mainly because of the energy loss by radiative cooling by H_3^+, CH and CH_3 produced photochemically. Heavier species other than H_2 cease to escape and only H_2 escapes when $CH_4/H_2 \gtrsim 0.01$. The maximum timescale for H_2 escape to satisfy the constraints of the isotopic compositions and the amount of volatiles on the present Earth becomes more than ~ 100 Myrs. Our results suggest that a hydrogen-rich reduced environment had been kept and played an important role in producing warm climate and organic matters linked to the emergence of life organisms on early Earth.

The difference in hydrodynamic escape rate of Mars from that of Earth is mainly due to the difference in the planetary mass and the gravity, despite weaker XUV flux at a larger distance from the Sun. The small gravity of Mars allows faster outflow to space

causing adiabatic cooling of expanding gas, leading to the lower atmospheric temperature and relatively inefficient radiative cooling. The higher hydrodynamic escape rate on Mars may have resulted in the observed paucity of volatiles on Mars compared to those on Earth.

Appendix A

Calculation method

A.1 CIP method

CIP method is one of numerical method to solve advection equations (Yabe and Aoki, 1991). One-dimensional advection equation is given by

$$\frac{\partial f}{\partial t} + v\frac{\partial f}{\partial x} = 0, \tag{A.1}$$

where t is the time, x is the position coordinate, f is a function of t and x, and v is the wave velocity. Differentiating equation (A.1),

$$\frac{\partial g}{\partial t} + v\frac{\partial g}{\partial x} = -g\frac{\partial v}{\partial x} \tag{A.2}$$

where g is the spatial derivative of f. Using these equations, we can trace the time evolution of f and g. If two values of f and g are given at two grid points, the profile between these points can be interpolated by the cubic polynomial

$$F_k(x_k) = a_k(x - x_k)^3 + b_k(x - x_k)^2 + c_k(x - x_k) + d_k. \tag{A.3}$$

The factors in equation (A.3) are given by

$$a_k = \frac{g_k + g_{kup}}{D^2} + \frac{2(f_k - f_{kup})}{D^3}, \tag{A.4}$$

$$b_k = \frac{3(f_{kup} - f_k)}{D^2} - \frac{2g_k + g_{kup}}{D}, \tag{A.5}$$

$$c_k = g_k, \tag{A.6}$$

$$d_k = f_k, \tag{A.7}$$

where $D = -\Delta x$, $kup = k - 1$ for $u \geq 0$ and $D = -\Delta x$, $kup = k + 1$ for $u < 0$. The profile at the $n + 1$ step can be obtained by shifting the profile by $u\Delta t$ so that

$$f_k^{n+1} = F(x - v\Delta t) = a_k\xi^3 + b_k\xi^2 + g_k^n\xi + f_k^n, \tag{A.8}$$

$$g_k^{n+1} = 3a_k\xi^2 + 2b_k\xi + g_k^n, \tag{A.9}$$

where $\xi = -v\Delta t$.

Next, we consider a hyperbolic equation:

$$\frac{\partial f}{\partial t} + \frac{\partial (vf)}{\partial x} = h, \tag{A.10}$$

where h is the source term. This equation can be expanded as follows:

$$\frac{\partial f}{\partial t} + v\frac{\partial f}{\partial x} = H. \tag{A.11}$$

where $H \equiv h - f\partial v/\partial x$. Differentiating equation (A.11),

$$\frac{\partial g}{\partial t} + v\frac{\partial g}{\partial x} = \frac{\partial H}{\partial x} - g\frac{\partial v}{\partial x}. \tag{A.12}$$

Equations (A.11) and (A.12) can be split into advection phases and nonadvection phases. The advection phases are given by

$$\frac{\partial f}{\partial t} + v\frac{\partial f}{\partial x} = 0, \tag{A.13}$$

$$\frac{\partial g}{\partial t} + v\frac{\partial g}{\partial x} = 0. \tag{A.14}$$

The nonadvection phases are given by

$$\frac{\partial f}{\partial t} = H, \tag{A.15}$$

$$\frac{\partial g}{\partial t} = \frac{\partial H}{\partial x} - g\frac{\partial v}{\partial x}. \tag{A.16}$$

The advection phases can be solved by CIP method. The nonadvection phases can be solved by a finite-difference method as follows:

$$f_k^{n+1} = f_k^* + H_k \Delta t, \tag{A.17}$$

$$\frac{g_k^{n+1} - g_k^*}{\Delta t} = \frac{f_{k+1}^{n+1} - f_{k-1}^{n+1} - f_{k+1}^* + f_{k-1}^*}{2\Delta x \Delta t} - g_i^* \frac{v_{k+1}^* - v_{k-1}^*}{2\Delta x}, \tag{A.18}$$

where values with * represents the values after solving the advection phases.

A.2 Application of CIP method to the fluid equations

The basic equations (2.1) (2.2) (2.3) can be described as follows:

$$\frac{\partial n_i}{\partial t} + u_i \frac{\partial n_i}{\partial r} = \omega_i - n_i \frac{\partial u_i}{\partial r} - \frac{2 n_i u_i}{r}, \tag{A.19}$$

$$\frac{\partial u_i}{\partial t} + u_i \frac{\partial u_i}{\partial r} = -\frac{1}{\rho_i}\frac{\partial p_i}{\partial r} - \frac{GM}{r^2} + \sum_j (u_j - u_i)\frac{\rho_j}{m_i + m_j} k_{ij}, \tag{A.20}$$

$$\frac{\partial p}{\partial t} + u \frac{\partial p}{\partial r} = -\frac{k_\gamma + 1}{k_\gamma} p \frac{\partial u}{\partial r} - \frac{2}{r}\frac{k_\gamma + 1}{k_\gamma} p u + \frac{1}{k_\gamma} q. \tag{A.21}$$

The advection phases are given by

$$\frac{\partial n_i}{\partial t} + u_i \frac{\partial n_i}{\partial r} = 0, \tag{A.22}$$

$$\frac{\partial u_i}{\partial t} + u_i \frac{\partial u_i}{\partial r} = 0, \tag{A.23}$$

$$\frac{\partial p}{\partial t} + u \frac{\partial p}{\partial r} = 0. \tag{A.24}$$

These advection phases can be solved by CIP method.

The nonadvection phases are given by

$$\frac{\partial n_i}{\partial t} = \omega_i - n_i \frac{\partial u_i}{\partial r} - \frac{2 n_i u_i}{r}, \tag{A.25}$$

$$\frac{\partial u_i}{\partial t} = -\frac{1}{\rho_i}\frac{\partial p_i}{\partial r} - \frac{GM}{r^2} + \sum_j (u_j - u_i)\frac{\rho_j}{m_i + m_j}k_{ij}, \tag{A.26}$$

$$\frac{\partial p}{\partial t} = -\frac{k_\gamma + 1}{k_\gamma}p\frac{\partial u}{\partial r} - \frac{2}{r}\frac{k_\gamma + 1}{k_\gamma}pu + \frac{1}{k_\gamma}q. \tag{A.27}$$

The nonadvection phases are solved by a finite-difference method. Here we adapted an approach that uses staggered meshes to solve these equations: n_i, ρ_i, and p are defined at the grid point r_i and u_i is defined at $x_{i+1/2}$. The vertical grids are set as follows:

$$r_k = r_0\left(\frac{r_N}{r_0}\right)^{(k/N)} \qquad (k = 0, 1, 2, ..., N) \tag{A.28}$$

where N is the number of grid and $N = 1000$ in this study.

First, the energy equation (A.27) is solved by a explicit method:

$$\frac{p_k^{n+1} - p_k^*}{\Delta t} = -\frac{k_{\gamma,k}^* + 1}{k_{\gamma,k}^*}p_k^*\frac{u_{k+1/2}^* - u_{k-1/2}^*}{\Delta r_{k-1/2}} - \frac{2}{r_k}\frac{k_{\gamma,k}^* + 1}{k_{\gamma,k}^*}p_k^* u_k^* + \frac{1}{k_{\gamma,k}^*}q_k. \tag{A.29}$$

Next, the continuity equations (A.25) are solved. The continuity equations are stiff equations in which some of the dependent variables change their values much more quickly than others. The change in the chemical source is much faster than those of the other therms. Here we use a semi-implicit method to reach steady state. The continuity equations are described in vector form as follows:

$$\frac{\partial \boldsymbol{n}}{\partial t} = \boldsymbol{F}_I + \boldsymbol{F}_E, \tag{A.30}$$

where $\boldsymbol{n} = (n_1, n_2, ..., n_N)$, $F_{I,i} = \omega_i$, and $F_{E,i} = -n_i\partial_r u_i - 2n_i u_i/r$. Approximating the time derivative by a simple forward difference,

$$\frac{\boldsymbol{n}^{n+1} - \boldsymbol{n}^*}{\Delta t} = \boldsymbol{F}_I^{n+1} + \boldsymbol{F}_E^*. \tag{A.31}$$

$\boldsymbol{F}_I^{n+1}$ is approximated by

$$\boldsymbol{F}_I^{n+1} \simeq \boldsymbol{F}_I^* + \left.\frac{\partial \boldsymbol{F}_I}{\partial \boldsymbol{n}}\right|_* (\boldsymbol{n}^{n+1} - \boldsymbol{n}^*), \tag{A.32}$$

$$\frac{\partial \boldsymbol{F}_I}{\partial \boldsymbol{n}} = \begin{pmatrix} \frac{\partial F_{I,1}}{\partial n_1} & \frac{\partial F_{I,1}}{\partial n_2} & \cdots & \frac{\partial F_{I,1}}{\partial n_N} \\ \frac{\partial F_{I,2}}{\partial n_1} & \frac{\partial F_{I,2}}{\partial n_2} & \cdots & \frac{\partial F_{I,2}}{\partial n_N} \\ \cdots & \cdots & \cdots & \cdots \\ \frac{\partial F_{I,N}}{\partial n_1} & \frac{\partial F_{I,N}}{\partial n_2} & \cdots & \frac{\partial F_{I,N}}{\partial n_N} \end{pmatrix} \tag{A.33}$$

Using this approximation,

$$\left(\frac{\boldsymbol{I}}{\Delta t} - \left.\frac{\partial \boldsymbol{F}_I}{\partial \boldsymbol{n}}\right|_*\right)(\boldsymbol{n}^{n+1} - \boldsymbol{n}^*) = \boldsymbol{F}_I^* + \boldsymbol{F}_E^*, \tag{A.34}$$

where $\boldsymbol{I}$ is the identity matrix. From this equation, the number densities at the next time step $\boldsymbol{n}^{n+1}$ can be calculated.

Finally, the motion equations are solved. The motion equations are also stiff because they include the momentum transfer terms among atmospheric species which change much more quickly than the other terms. Thus, we use a implicit method as follows:

$$\frac{u_{i,k+1/2}^{n+1} - u_{i,k+1/2}^*}{\Delta t} = -\frac{1}{\rho_{i,k+1/2}^{n+1}} \frac{p_{i,k+1}^{n+1} - p_{i,k}^{n+1} + \nu_{i,k+1}^{n+1} - \nu_{i,k}^{n+1}}{\Delta r_k} - \frac{GM}{r_{k+1/2}^2} + \sum_j (u_{j,k+1/2}^{n+1} - u_{i,k+1/2}^{n+1}) \frac{\rho_{j,k+1/2}^{n+1}}{m_i + m_j} k_{ij,k+1/2}^{n+1}, \tag{A.35}$$

where $\nu_{i,k}^n$ is the numerical viscosity and given by

$$\nu_{i,k}^n = \begin{cases} -c_\nu \gamma_i \rho_{i,k}^n (u_{i,k+1/2}^n - u_{i,k-1/2}^n) \left[\sqrt{\frac{p_{i,k}^n}{\rho_{i,k}^n}} - \frac{\gamma_i + 1}{2}(u_{i,k+1/2}^n - u_{i,k-1/2}^n)\right] & (u_{i,k+1/2}^n - u_{i,k-1/2}^n < 0) \\ 0 & (u_{i,k+1/2}^n - u_{i,k-1/2}^n \geq 0) \end{cases} \tag{A.36}$$

where c_ν is the numerical viscosity coefficient and we adapt $c_\nu = 0.9$. Eauations (A.34) can be written by

$$\boldsymbol{A}_{\mathrm{mom}} \boldsymbol{u}^{n+1} = \boldsymbol{B}_{\mathrm{mom}}, \tag{A.37}$$

$$A_{\mathrm{mom}}(i,j) = -\rho_{j,k+1/2}^{n+1} \frac{k_{ij,k+1/2}^{n+1}}{m_i + m_j} \Delta t,\ A_{\mathrm{mom}}(i,i) = 1 - \sum_{j \neq i} A_{\mathrm{mom}}(i,j), \tag{A.38}$$

$$B_{\mathrm{mom}}(i) = u_{i,k+1/2}^* - \frac{1}{\rho_{i,k+1/2}^{n+1}} \frac{p_{i,k+1}^{n+1} - p_{i,k}^{n+1} + \nu_{i,k+1}^{n+1} - \nu_{i,k}^{n+1}}{\Delta r_k} \Delta t - \frac{GM}{r_{k+1/2}^2} \Delta t. \tag{A.39}$$

$\boldsymbol{u}^{n+1}$ can be calculated by solving the matrix (A.39).

The time step is defined to satisfy the CFL condition:

$$\Delta t = \nu \min\left\{\frac{\Delta r_k}{c_k}\right\}, \tag{A.40}$$

where ν is the Courant number, and c_k is the magnitude of the velocity.

Convergence to a steady state is measured by the normalized difference of all variables between time steps:

$$\Delta Q = \sqrt{\frac{1}{N_{\mathrm{var}}} \sum_{k=1}^{N_{\mathrm{var}}} \left[\frac{1}{N_{\mathrm{grid}}} \sum_{\mathrm{grid}=1}^{N_{\mathrm{grid}}} \frac{(Q_k^{n+1} - Q_k^n)^2}{(Q_k^n)^2} \right]}, \tag{A.41}$$

where Q_k^n is the variables, N_{var} is the number of variables in the system, and N_{grid} is the number of grid cells in the system. The steady state tolerance is set at $\Delta Q < 10^{-10}$.

Acknowledgements

First, I would like to show my deepest gratitude to my supervisor Prof. Kiyoshi Kuramoto. He always took much time to discuss my work with me. Without his instructive comments and encouragement, I would not be able to complete this thesis.

I acknowledge members of Planetary and Space Group. I have received a lot of assistances from them. I also thank EPnetFaN members for providing us with the computational environment.

I also appreciate financial support by Grant-in-Aid for JSPS Research Fellow.

Finally, I am grateful to my parents and grandparents for their enduring encouragements and supports.

Bibliography

[1] P. M. Banks and G. Kockarts. *Aeronomy, part B.* Academic Press, New York, 1973.

[2] NZ Boctor, CM O ' DAlexander, J Wang, E Hauri. The sources of water in martian meteorites: Clues from hydrogen isotopes. *Geochimica et Cosmochimica Acta*, Vol. 67, No. 20, pp. 3971–3989, 2003.

[3] William V Boynton, DW Ming, SP Kounaves, SMM Young, RE Arvidson, MH Hecht, J Hoffman, PB Niles, DK Hamara, RC Quinn, et al. Evidence for calcium carbonate at the mars phoenix landing site. *Science*, Vol. 325, No. 5936, pp. 61–64, 2009.

[4] J. I. Castor. *Radiation hydrodynamics.* 2004.

[5] David C Catling and James F Kasting. *Atmospheric evolution on inhabited and lifeless worlds.* Cambridge University Press, 2017.

[6] JE Chambers and GW Wetherill. Making the terrestrial planets: N-body integrations of planetary embryos in three dimensions. *Icarus*, Vol. 136, No. 2, pp. 304–327, 1998.

[7] E Chassefière. Hydrodynamic escape of hydrogen from a hot water-rich atmosphere: The case of venus. *Journal of Geophysical Research: Planets*, Vol. 101, No. E11, pp. 26039–26056, 1996.

[8] M. W. Claire, J. Sheets, M. Cohen, I. Ribas, V. S. Meadows, and D. C. Catling. The evolution of solar flux from 0.1 nm to 160 μ m: quantitative estimates for planetary studies. *The Astrophysical Journal*, Vol. 757(1), pp. 95–107, 2012.

[9] Robert A Craddock and Alan D Howard. The case for rainfall on a warm, wet early mars. *Journal of Geophysical Research: Planets*, Vol. 107, No. E11, pp. 21–1, 2002.

[10] N Dauphas and A Pourmand. Hf–w–th evidence for rapid growth of mars and its status as a planetary embryo. *Nature*, Vol. 473, p. 489, 2011.

[11] Nicolas Dauphas. The isotopic nature of the earth ' s accreting material through time. *Nature*, Vol. 541, No. 7638, pp. 521–524, 2017.

[12] David J Des Marais. Isotopic evolution of the biogeochemical carbon cycle during the precambrian. *Reviews in Mineralogy and Geochemistry*, Vol. 43, No. 1, pp. 555–578, 2001.

[13] G. Dreibus and H. Wänke. Volatiles on earth and mars: A comparison. *Icarus*, Vol. 71(2), pp. 225–240, 1987.

[14] Jennifer L Eigenbrode, Roger E Summons, Andrew Steele, Caroline Freissinet, Maëva Millan, Rafael Navarro-González, Brad Sutter, Amy C McAdam, Heather B Franz, Daniel P Glavin, et al. Organic matter preserved in 3-billion-year-old mudstones at gale crater, mars. *Science*, Vol. 360, No. 6393, pp. 1096–1101, 2018.

[15] Linda T Elkins-Tanton. Linked magma ocean solidification and atmospheric growth for earth and mars. *Earth and Planetary Science Letters*, Vol. 271, No. 1-4, pp. 181–191, 2008.

[16] N. V. Erkaev, H. Lammer, L. T. Elkins-Tanton, A. Stökl, P. Odert, Emmanuel. Marcq, E. A. Dorfi, K. G. Kislyakova, Y. N. Kulikov, M. Leitzinger, et al. Escape of the martian protoatmosphere and initial water inventory. *Planetary and space science*, Vol. 98, pp. 106–119, 2014.

[17] Nikolai V Erkaev, Helmut Lammer, Petra Odert, Yuri N Kulikov, Kristina G Kislyakova, Maxim L Khodachenko, Manuel Güdel, Arnold Hanslmeier, and Helfried Biernat. Xuv-exposed, non-hydrostatic hydrogen-rich upper atmospheres of terrestrial planets. part i: atmospheric expansion and thermal escape. *Astrobiology*, Vol. 13, No. 11, pp. 1011–1029, 2013.

[18] NV Erkaev, H Lammer, P Odert, KG Kislyakova, CP Johnstone, M Güdel, and ML Khodachenko. Euv-driven mass-loss of protoplanetary cores with hydrogen-dominated atmospheres: the influences of ionization and orbital distance. *Monthly Notices of the Royal Astronomical Society*, Vol. 460, No. 2, pp. 1300–1309, 2016.

[19] Mario Fischer-Gödde, Bo-Magnus Elfers, Carsten Münker, Kristoffer Szilas, Wolfgang D Maier, Nils Messling, Tomoaki Morishita, Martin Van Kranendonk, and Hugh Smithies. Ruthenium isotope vestige of earth ' s pre-late-veneer mantle preserved in archaean rocks. *Nature*, Vol. 579, No. 7798, pp. 240–244, 2020.

[20] Mario Fischer-Gödde and Thorsten Kleine. Ruthenium isotopic evidence for an inner solar system origin of the late veneer. *Nature*, Vol. 541, No. 7638, pp. 525–527, 2017.

[21] Evelyn Füri and Bernard Marty. Nitrogen isotope variations in the solar system. *Nature Geoscience*, Vol. 8, No. 7, pp. 515–522, 2015.

[22] Johannes Geiss and George Gloeckler. Abundances of deuterium and helium-3 in the protosolar cloud. In *Primordial Nuclei and their Galactic evolution*, pp. 239–250. Springer, 1998.

[23] Hidenori Genda. Origin of earth ' s oceans: An assessment of the total amount, history and supply of water. *Geochemical Journal*, Vol. 50, No. 1, pp. 27–42, 2016.

[24] Hidenori Genda and Yutaka Abe. Survival of a proto-atmosphere through the stage of giant impacts: the mechanical aspects. *Icarus*, Vol. 164, No. 1, pp. 149–162, 2003.

[25] Hidenori Genda and Yutaka Abe. Enhanced atmospheric loss on protoplanets at the giant impact phase in the presence of oceans. *Nature*, Vol. 433, No. 7028, pp. 842–844, 2005.

[26] DO Gough. Solar interior structure and luminosity variations. In *Physics of Solar Variations*, pp. 21–34. Springer, 1981.

[27] Monica M Grady and Ian P Wright. Elemental and isotopic abundances of carbon and nitrogen in meteorites. *Space Science Reviews*, Vol. 106, No. 1-4, pp. 231–248, 2003.

[28] Manuel Güdel. The sun in time: Activity and environment. *Living Reviews in Solar Physics*, Vol. 4, No. 1, p. 3, 2007.

[29] Manuel Guedel, Edward F Guinan, and Stephen L Skinner. The x-ray sun in time: a study of the long-term evolution of coronae of solar-type stars. *The Astrophysical Journal*, Vol. 483, No. 2, p. 947, 1997.

[30] George L Hashimoto, Yutaka Abe, and Seiji Sugita. The chemical composition of the early terrestrial atmosphere: Formation of a reducing atmosphere from ci-like material. *Journal of Geophysical Research: Planets*, Vol. 112, No. E5, 2007.

[31] Ch Hayashi, K Nakazawa, and Y Nakagawa. Formation of the solar system. In *Protostars and planets II*, pp. 1100–1153, 1985.

[32] Paul Henderson, Gideon M Henderson, et al. *The Cambridge handbook of earth science data*. Cambridge University Press Cambridge, 2009.

[33] Marc M Hirschmann. Comparative deep earth volatile cycles: The case for c recycling from exosphere/mantle fractionation of major (h2o, c, n) volatiles and from h2o/ce, co2/ba, and co2/nb exosphere ratios. *Earth and Planetary Science Letters*, Vol. 502, pp. 262–273, 2018.

[34] Heinrich D Holland. The chemistry of the atmosphere and oceans-(v. 1). 1978.

[35] WF Huebner and J Mukherjee. Photoionization and photodissociation rates in solar and blackbody radiation fields. *Planetary and Space Science*, Vol. 106, pp. 11–45, 2015.

[36] Donald M Hunten, Robert O Pepin, and James CG Walker. Mass fractionation in hydrodynamic escape. *Icarus*, Vol. 69, No. 3, pp. 532–549, 1987.

[37] Masahiro Ikoma and Hidenori Genda. Constraints on the mass of a habitable planet with water of nebular origin. *The Astrophysical Journal*, Vol. 648, No. 1, p. 696, 2006.

[38] BM Jakosky, David Brain, Michael Chaffin, S Curry, Justin Deighan, Joseph Grebowsky, Jasper Halekas, François Leblanc, Robert Lillis, JG Luhmann, et al. Loss of the martian atmosphere to space: Present-day loss rates determined from maven observations and integrated loss through time. *Icarus*, Vol. 315, pp. 146–157, 2018.

[39] Bruce M Jakosky, Robert O Pepin, Robert E Johnson, and Jane L Fox. Mars atmospheric loss and isotopic fractionation by solar-wind-induced sputtering and photochemical escape. *Icarus*, Vol. 111, No. 2, pp. 271–288, 1994.

[40] Ben Johnson and Colin Goldblatt. The nitrogen budget of earth. *Earth-Science Reviews*, Vol. 148, pp. 150–173, 2015.

[41] James F Kasting. Co2 condensation and the climate of early mars. *icarus*, Vol. 94, No. 1, pp. 1–13, 1991.

[42] James F Kasting and James B Pollack. Loss of water from venus. i. hydrodynamic escape of hydrogen. *Icarus*, Vol. 53, No. 3, pp. 479–508, 1983.

[43] James F Kasting, Kevin J Zahnle, and James CG Walker. Photochemistry of methane in the earth's early atmosphere. *Precambrian Research*, Vol. 20, No. 2-4, pp. 121–148, 1983.

[44] John F Kerridge. Carbon, hydrogen and nitrogen in carbonaceous chondrites: Abundances and isotopic compositions in bulk samples. *Geochimica et Cosmochimica Acta*, Vol. 49, No. 8, pp. 1707–1714, 1985.

[45] NT Kita, GR Huss, S Tachibana, Yuri Amelin, LE Nyquist, and Ian D Hutcheon. Constraints on the origin of chondrules and cais from short-lived and long-lived radionuclides. In *Chondrites and the protoplanetary disk*, Vol. 341, p. 558, 2005.

[46] Mizuho Koike, Ryoichi Nakada, Iori Kajitani, Tomohiro Usui, Yusuke Tamenori, Haruna Sugahara, and Atsuko Kobayashi. In-situ preservation of nitrogen-bearing organics in noachian martian carbonates. *Nature Communications*, Vol. 11, No. 1, pp. 1–7, 2020.

[47] Eiichiro Kokubo and Shigeru Ida. Oligarchic growth of protoplanets. *Icarus*, Vol. 131, No. 1, pp. 171–178, 1998.

[48] TT Koskinen, MJ Harris, RV Yelle, and P Lavvas. The escape of heavy atoms from the ionosphere of hd209458b. i. a photochemical–dynamical model of the thermosphere. *Icarus*, Vol. 226, No. 2, pp. 1678–1694, 2013.

[49] Vladimir M Krasnopolsky, William H Gemmill, and Laurence C Breaker. A neural network multiparameter algorithm for ssm/i ocean retrievals: Comparisons and validations. *Remote sensing of environment*, Vol. 73, No. 2, pp. 133–142, 2000.

[50] Yu N Kulikov, H Lammer, HIM Lichtenegger, N Terada, I Ribas, C Kolb, D Langmayr, R Lundin, EF Guinan, S Barabash, et al. Atmospheric and water loss from early venus. *Planetary and Space Science*, Vol. 54, No. 13-14, pp. 1425–1444, 2006.

[51] Kiyoshi Kuramoto. Accretion, core formation, h and c evolution of the earth and mars. *Physics of the Earth and Planetary Interiors*, Vol. 100, No. 1-4, pp. 3–20, 1997.

[52] Kiyoshi Kuramoto and Takafumi Matsui. Partitioning of h and c between the mantle and core during the core formation in the earth: Its implications for the

atmospheric evolution and redox state of early mantle. *Journal of Geophysical Research: Planets*, Vol. 101, No. E6, pp. 14909–14932, 1996.

[53] Kiyoshi Kuramoto, Takafumi Umemoto, and Masaki Ishiwatari. Effective hydrodynamic hydrogen escape from an early earth atmosphere inferred from high-accuracy numerical simulation. *Earth and Planetary Science Letters*, Vol. 375, pp. 312–318, 2013.

[54] H. Lammer, E. Chassefière, Ö. Karatekin, A. Morschhauser, P. B. Niles, O. Mousis, P. Odert, U. V. Möstl, D. Breuer, Vé. Dehant, et al. Outgassing history and escape of the martian atmosphere and water inventory. *Space Science Reviews*, Vol. 174(1-4), pp. 113–154, 2013.

[55] H Lammer, A Stökl, NV Erkaev, EA Dorfi, P Odert, M Güdel, Yu N Kulikov, KG Kislyakova, and M Leitzinger. Origin and loss of nebula-captured hydrogen envelopes from 'sub'-to 'super-earths' in the habitable zone of sun-like stars. *Monthly Notices of the Royal Astronomical Society*, Vol. 439, No. 4, pp. 3225–3238, 2014.

[56] TJ Lapen, M Righter, AD Brandon, Vinciane Debaille, BL Beard, JT Shafer, and AH Peslier. A younger age for alh84001 and its geochemical link to shergottite sources in mars. *Science*, Vol. 328, No. 5976, pp. 347–351, 2010.

[57] YH Le Teuff, TJ Millar, and AJ Markwick. The umist database for astrochemistry 1999. *Astronomy and Astrophysics Supplement Series*, Vol. 146, No. 1, pp. 157–168, 2000.

[58] Christophe Lécuyer, Philippe Gillet, and François Robert. The hydrogen isotope composition of seawater and the global water cycle. *Chemical Geology*, Vol. 145, No. 3-4, pp. 249–261, 1998.

[59] Kuo-Nan Liou. *An introduction to atmospheric radiation*, Vol. 84. Elsevier, 2002.

[60] Katharina Lodders. Solar system abundances of the elements. In *Principles and perspectives in cosmochemistry*, pp. 379–417. Springer, 2010.

[61] Bernard Marty. The origins and concentrations of water, carbon, nitrogen and noble gases on earth. *Earth and Planetary Science Letters*, Vol. 313, pp. 56–66, 2012.

[62] Bernard Marty, Conel M O ' DAlexander, Sean N Raymond. Primordial origins of earth ' s carbon. *Reviews in Mineralogy and Geochemistry*, Vol. 75, No. 1, pp. 149–181, 2013.

[63] Takafumi Matsui and Yutaka Abe. Evolution of an impact-induced atmosphere and magma ocean on the accreting earth. *Nature*, Vol. 319, No. 6051, pp. 303–305, 1986.

[64] D McElroy, C Walsh, AJ Markwick, MA Cordiner, K Smith, and TJ Millar. The umist database for astrochemistry 2012. *Astronomy & Astrophysics*, Vol. 550, p. A36, 2013.

[65] Stephen J Mojzsis, T Mark Harrison, and Robert T Pidgeon. Oxygen-isotope evidence from ancient zircons for liquid water at the earth's surface 4,300 myr ago. *Nature*, Vol. 409, No. 6817, pp. 178–181, 2001.

[66] A. G. Munoz. Physical and chemical aeronomy of hd 209458b. *Planetary and Space Science*, Vol. 55(10), pp. 1426–1455, 2007.

[67] Kiyoshi Nakazawa, Hiroshi Mizuno, Minoru Sekiya, and Chushiro Hayashi. Structure of the primordial atmosphere surrounding the early-earth. *Journal of geomagnetism and geoelectricity*, Vol. 37, No. 8, pp. 781–799, 1985.

[68] Paul B Niles, David C Catling, Gilles Berger, Eric Chassefière, Bethany L Ehlmann, Joseph R Michalski, Richard Morris, Steven W Ruff, and Brad Sutter. Geochemistry of carbonates on mars: implications for climate history and nature of aqueous environments. *Space Science Reviews*, Vol. 174, No. 1-4, pp. 301–328, 2013.

[69] Petra Odert, Helmut Lammer, Nikolai V Erkaev, Athanasia Nikolaou, Herbert IM Lichtenegger, Colin P Johnstone, Kristina G Kislyakova, Martin Leitzinger, and Nicola Tosi. Escape and fractionation of volatiles and noble gases from mars-sized planetary embryos and growing protoplanets. *Icarus*, Vol. 307, pp. 327–346, 2018.

[70] Kaveh Pahlevan, Laura Schaefer, and Marc M Hirschmann. Hydrogen isotopic evidence for early oxidation of silicate earth. *Earth and Planetary Science Letters*, Vol. 526, p. 115770, 2019.

[71] Robert O Pepin. On the origin and early evolution of terrestrial planet atmospheres and meteoritic volatiles. *Icarus*, Vol. 92, No. 1, pp. 2–79, 1991.

[72] Ramses M Ramirez and Robert A Craddock. The geological and climatological case for a warmer and wetter early mars. *Nature Geoscience*, Vol. 11, No. 4, p. 230, 2018.

[73] Ramses M Ramirez, Ravi Kopparapu, Michael E Zugger, Tyler D Robinson, Richard Freedman, and James F Kasting. Warming early mars with co 2 and h 2. *Nature Geoscience*, Vol. 7, No. 1, p. 59, 2014.

[74] I. Ribas, E. F. Guinan, M. Gudel, and M. Audard. Evolution of the solar activity over time and effects on planetary atmospheres. i. high-energy irradiances (1-1700 å). *The Astrophysical Journal*, Vol. 622(1), pp. 680–694, 2005.

[75] Pascal Richet, Yan Bottinga, and Marc Javoy. A review of hydrogen, carbon, nitrogen, oxygen, sulphur, and chlorine stable isotope fractionation among gaseous molecules. *Annual Review of Earth and Planetary Sciences*, Vol. 5, No. 1, pp. 65–110, 1977.

[76] Minik T Rosing. 13c-depleted carbon microparticles in¿ 3700-ma sea-floor sedimentary rocks from west greenland. *Science*, Vol. 283, No. 5402, pp. 674–676, 1999.

[77] H. Saito and K. Kuramoto. Formation of a hybrid-type proto-atmosphere on mars accreting in the solar nebula. *Monthly Notices of the Royal Astronomical Society*, Vol. 475(1), pp. 1274–1287, 2018.

[78] Gordon Schlesinger and Stanley L Miller. Prebiotic synthesis in atmospheres containing ch 4, co, and co 2. *Journal of molecular evolution*, Vol. 19, No. 5, pp. 383–390, 1983.

[79] Minoru Sekiya, Kiyoshi Nakazawa, and Chushiro Hayashi. Dissipation of the primordial terrestrial atmosphere due to irradiation of the solar euv. *Progress of Theoretical Physics*, Vol. 64, No. 6, pp. 1968–1985, 1980.

[80] H. Tang and N. Dauphas. 60fe–60ni chronology of core formation in mars. *Earth and Planetary Science Letters*, Vol. 390, pp. 264–274, 2014.

[81] F. Tian, O. B. Toon, A. A. Pavlov, and H. De Sterck. A hydrogen-rich early earth atmosphere. *Science*, Vol. 308, pp. 1014–1017, 2005.

[82] F. Tian, O. B. Toon, A. A. Pavlov, and H. De Sterck. Transonic hydrodynamic escape of hydrogen from extrasolar planetary atmospheres. *The Astrophysical Journal*, Vol. 621, p. 1049, 2005.

[83] Feng Tian, James F Kasting, Han-Li Liu, and Raymond G Roble. Hydrodynamic planetary thermosphere model: 1. response of the earth's thermosphere to extreme solar euv conditions and the significance of adiabatic cooling. *Journal of Geophysical Research: Planets*, Vol. 113, No. E5, 2008.

[84] Feng Tian, James F Kasting, and Stanley C Solomon. Thermal escape of carbon from the early martian atmosphere. *Geophysical Research Letters*, Vol. 36, No. 2, 2009.

[85] L. Tu, C. P. Johnstone, M. Güdel, and H. Lammer. The extreme ultraviolet and x-ray sun in time: High-energy evolutionary tracks of a solar-like star. *Astronomy & Astrophysics*, Vol. 577, p. L3, 2015.

[86] Lin Tu, Colin P Johnstone, Manuel Güdel, and Helmut Lammer. The extreme ultraviolet and x-ray sun in time: high-energy evolutionary tracks of a solar-like star. *Astronomy & Astrophysics*, Vol. 577, p. L3, 2015.

[87] Tomohiro Usui, Conel MO'D Alexander, Jianhua Wang, Justin I Simon, and John H Jones. Origin of water and mantle–crust interactions on mars inferred from hydrogen isotopes and volatile element abundances of olivine-hosted melt inclusions of primitive shergottites. *Earth and Planetary Science Letters*, Vol. 357, pp. 119–129, 2012.

[88] Ann M Vickery and H Jay Melosh. Atmospheric erosion and impactor retention in large impacts, with application to mass extinctions. *Global catastrophes in Earth history*, Vol. 247, pp. 289–300, 1990.

[89] GL Villanueva, MJ Mumma, RE Novak, HU Käufl, P Hartogh, T Encrenaz, A Tokunaga, A Khayat, and MD Smith. Strong water isotopic anomalies in the martian atmosphere: Probing current and ancient reservoirs. *Science*, Vol. 348, No. 6231, pp. 218–221, 2015.

[90] Richard J Walker, Katherine Bermingham, Jingao Liu, Igor S Puchtel, Mathieu Touboul, and Emily A Worsham. In search of late-stage planetary building blocks. *Chemical Geology*, Vol. 411, pp. 125–142, 2015.

[91] Andrew J Watson, Thomas M Donahue, and James CG Walker. The dynamics of a rapidly escaping atmosphere: applications to the evolution of earth and venus. *Icarus*, Vol. 48, No. 2, pp. 150–166, 1981.

[92] EH Wilson and SK Atreya. Chemical sources of haze formation in titan's atmosphere. *Planetary and Space Science*, Vol. 51, No. 14-15, pp. 1017–1033, 2003.

[93] N. J. Wright, J. J. Drake, E. E. Mamajek, and G. W. Henry. The stellar-activity-rotation relationship and the evolution of stellar dynamos. *The Astrophysical Journal*, Vol. 743(1), pp. 48–64, 2011.

[94] Takashi Yabe and T Aoki. A universal solver for hyperbolic equations by cubic-polynomial interpolation i. one-dimensional solver. *Computer Physics Communications*, Vol. 66, pp. 219–232, 1991.

[95] Roger V Yelle. Aeronomy of extra-solar giant planets at small orbital distances. *Icarus*, Vol. 170, pp. 167–179, 2004.

[96] Tatsuya Yoshida and Kiyoshi Kuramoto. Sluggish hydrodynamic escape of early martian atmosphere with reduced chemical compositions. *Icarus*, p. 113740, 2020.

[97] Yuk L Yung and William B DeMore. *Photochemistry of planetary atmospheres*. Oxford University Press, 1998.

[98] K. Zahnle, J. F. Kasting, and J. B. Pollack. Mass fractionation of noble gases in diffusion-limited hydrodynamic hydrogen escape. *Icarus*, Vol. 84.2, pp. 502–527, 1990.

[99] Kevin J Zahnle, Marko Gacesa, and David C Catling. Strange messenger: A new history of hydrogen on earth, as told by xenon. *Geochimica et Cosmochimica Acta*, Vol. 244, pp. 56–85, 2019.

[100] Kevin J Zahnle and James F Kasting. Mass fractionation during transonic escape and implications for loss of water from mars and venus. *Icarus*, Vol. 68, No. 3, pp. 462–480, 1986.

[101] Kevin J Zahnle, Roxana Lupu, David C Catling, and Nick Wogan. Creation and evolution of impact-generated reduced atmospheres of early earth. *The Planetary Science Journal*, Vol. 1, No. 1, p. 11, 2020.